Nature cell biology

Reversible amyloids of pyruvate kinase couple cell metabolism and stress granule disassembly

Gea Cereghetti [1,2], Caroline Wilson-Zbinden[1,8], Vera M. Kissling [1,3,8], Maren Diether[4], Alexandra Arm[1], Haneul Yoo[5], Ilaria Piazza[4,6], Shady Saad [1,7], Paola Picotti[4], D. Allan Drummond [5], Uwe Sauer[4], Reinhard Dechant [1] and Matthias Peter [1]✉

Cells respond to stress by blocking translation, rewiring metabolism and forming transient messenger ribonucleoprotein assemblies called stress granules (SGs). After stress release, re-establishing homeostasis and disassembling SGs requires ATP-consuming processes. However, the molecular mechanisms whereby cells restore ATP production and disassemble SGs after stress remain poorly understood. Here we show that upon stress, the ATP-producing enzyme Cdc19 forms inactive amyloids, and that their rapid re-solubilization is essential to restore ATP production and disassemble SGs in glucose-containing media. Cdc19 re-solubilization is initiated by the glycolytic metabolite fructose-1,6-bisphosphate, which directly binds Cdc19 amyloids, allowing Hsp104 and Ssa2 chaperone recruitment and aggregate re-solubilization. Fructose-1,6-bisphosphate then promotes Cdc19 tetramerization, which boosts its activity to further enhance ATP production and SG disassembly. Together, these results describe a molecular mechanism that is critical for stress recovery and directly couples cellular metabolism with SG dynamics via the regulation of reversible Cdc19 amyloids.

To maintain homeostasis, cells need to rapidly sense stress conditions, such as heat stress and nutrient starvation, and orchestrate the appropriate protective responses, including the formation of stress granules (SGs)[1]. Stress granules are reversible, membrane-less messenger ribonucleoprotein organelles that form in the cytoplasm in response to metabolic stress and are thought to store and protect messenger RNA and proteins from stress-induced degradation[1-6]. The formation of persistent SGs due to chronic stress or mutations and the consequent metabolic changes have been associated with neurodegenerative diseases such as amyotrophic lateral sclerosis and Alzheimer's disease[7,8]. Thus, SGs must be tightly controlled and efficiently disassembled. However, despite their patho-physiological importance, the mechanisms regulating SG dynamics remain poorly understood.

Most SG proteins contain intrinsically disordered low-complexity regions (LCRs) that can condense by liquid–liquid phase separation[9,10]. This process, together with low-affinity RNA–RNA interactions, is thought to underlie SG formation[11,12]. In contrast, SG disassembly mechanisms are less well understood. ATP plays a crucial role in disassembly, as artificial ATP depletion reduces SG dynamics and results in persistent SGs[3,9,13], whereas the addition of ATP to stressed cells triggers aggregate disassembly[14]. The ATP-dependent activities of the disaggregase Hsp104 and the Hsp70 chaperones Ssa1 and Ssa2 as well as the kinases Sky1 (ref. [15]) and ULK1/2 (ref.[16]) have been implicated in efficient SG disassembly and growth restart after stress[14,17]. ATP itself was also proposed to act as a biological hydrotrope, modulating cytoplasmic diffusion and further facilitating aggregate re-solubilization[18]. However, ATP reserves are rapidly depleted in stressed cells[14,19-22], raising the question of how energy production is restored for efficient post-stress SG disassembly.

Yeast cells mainly produce ATP by fermenting glucose through glycolysis[23,24], in which the conserved enzyme pyruvate kinase (Cdc19) catalyses the ATP-producing and irreversible final step— that is the conversion of phosphoenolpyruvate (PEP) and ADP into pyruvate and ATP. Cdc19 activity is modulated by its allosteric regulator fructose-1,6-bisphosphate (FBP), which promotes Cdc19 oligomerization into more active tetramers[4,22,25,26]. Moreover, glycolytic flux is altered by trehalose metabolism, which regulates glucose-6-phosphate (G6P) availability and hexokinase activity[27-29]. We previously demonstrated that Cdc19 reversibly aggregates via its LCR and localizes to SGs in response to glucose starvation and heat stress[4,30]. The formation and disassembly of Cdc19 aggregates modulate SG dynamics and ensure stress survival. In particular, failure to timely re-solubilize Cdc19 aggregates results in persistent SGs and no cell-cycle restart after stress release. However, how physiological Cdc19 aggregates are re-solubilized and how they regulate SG disassembly is unclear.

To address these questions, we combined in vitro and in vivo approaches and exploited a Cdc19 mutant (Cdc19[irrev]) that is unable to disassemble Cdc19 aggregates after stress[4]. We found that reversible Cdc19 aggregates assume an enzymatically inactive amyloid structure in vivo. Their post-stress re-solubilization is necessary to restore ATP production and re-solubilize SGs on fermentable carbon sources. We propose a molecular mechanism in which direct FBP binding to functional Cdc19 aggregates initiates their re-solubilization and subsequent SG disassembly by promoting the recruitment of the molecular chaperones Hsp104 and Ssa2. Together, our results not only provide a mechanism for re-solubilizing functional amyloids in vivo but also show how metabolism and energy production are coupled to SG dynamics and cell growth.

[1]Institute of Biochemistry, Department of Biology, ETH Zurich, Zurich, Switzerland. [2]PhD Program for Molecular Life Sciences, Life Science Zurich, Zurich, Switzerland. [3]PhD Program for Biomolecular Structure and Mechanism, Life Science Zurich, Zurich, Switzerland. [4]Institute of Molecular Systems Biology, ETH Zurich, Zurich, Switzerland. [5]Department of Biochemistry and Molecular Biology, University of Chicago, Chicago, IL, USA. [6]Present address: Max Delbrück Center for Molecular Medicine, Berlin, Germany. [7]Present address: Department of Chemical and Systems Biology, Stanford University, Stanford, CA, USA. [8]These authors contributed equally: Caroline Wilson-Zbinden, Vera M. Kissling. ✉e-mail: matthias.peter@bc.biol.ethz.ch
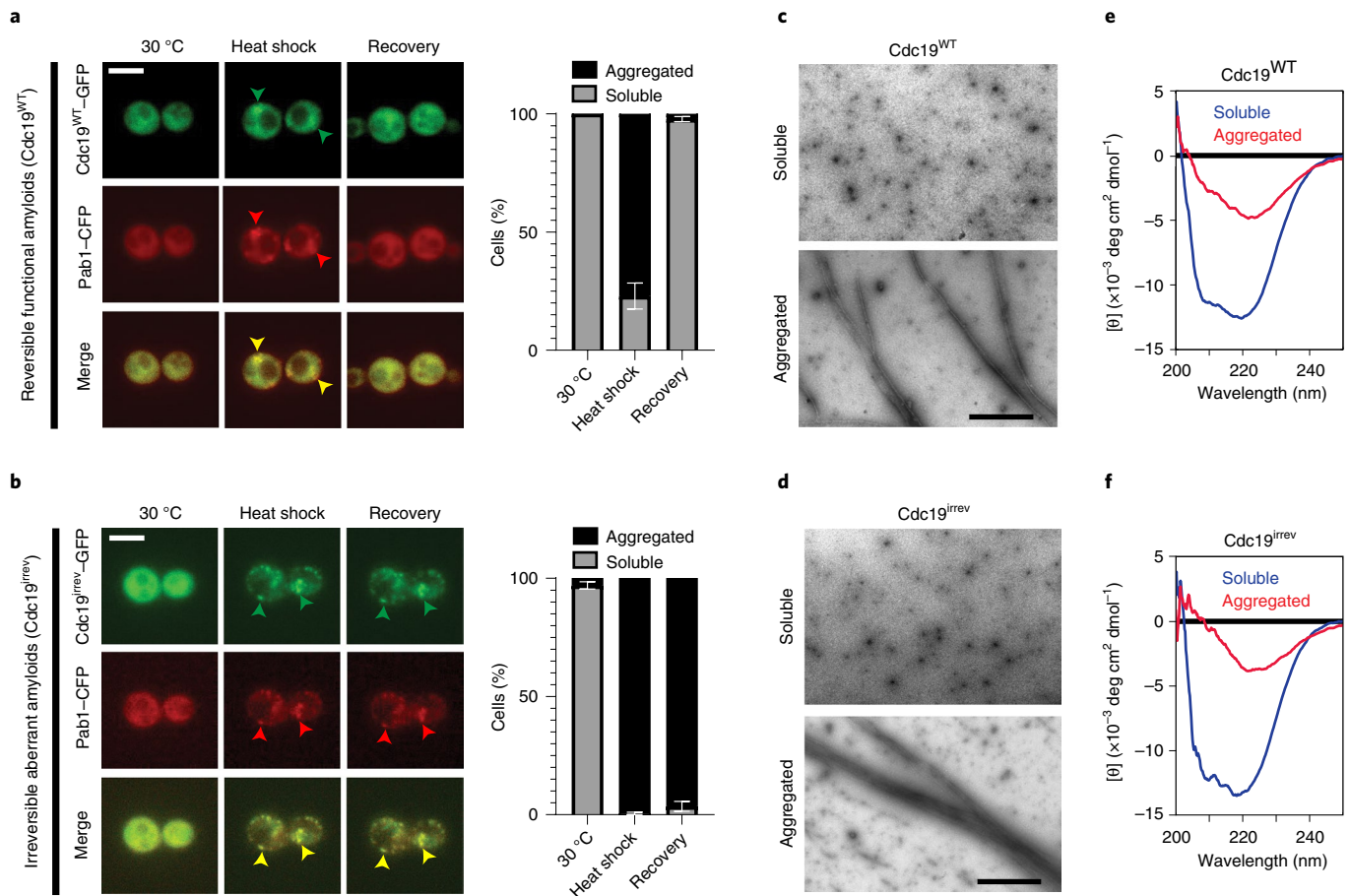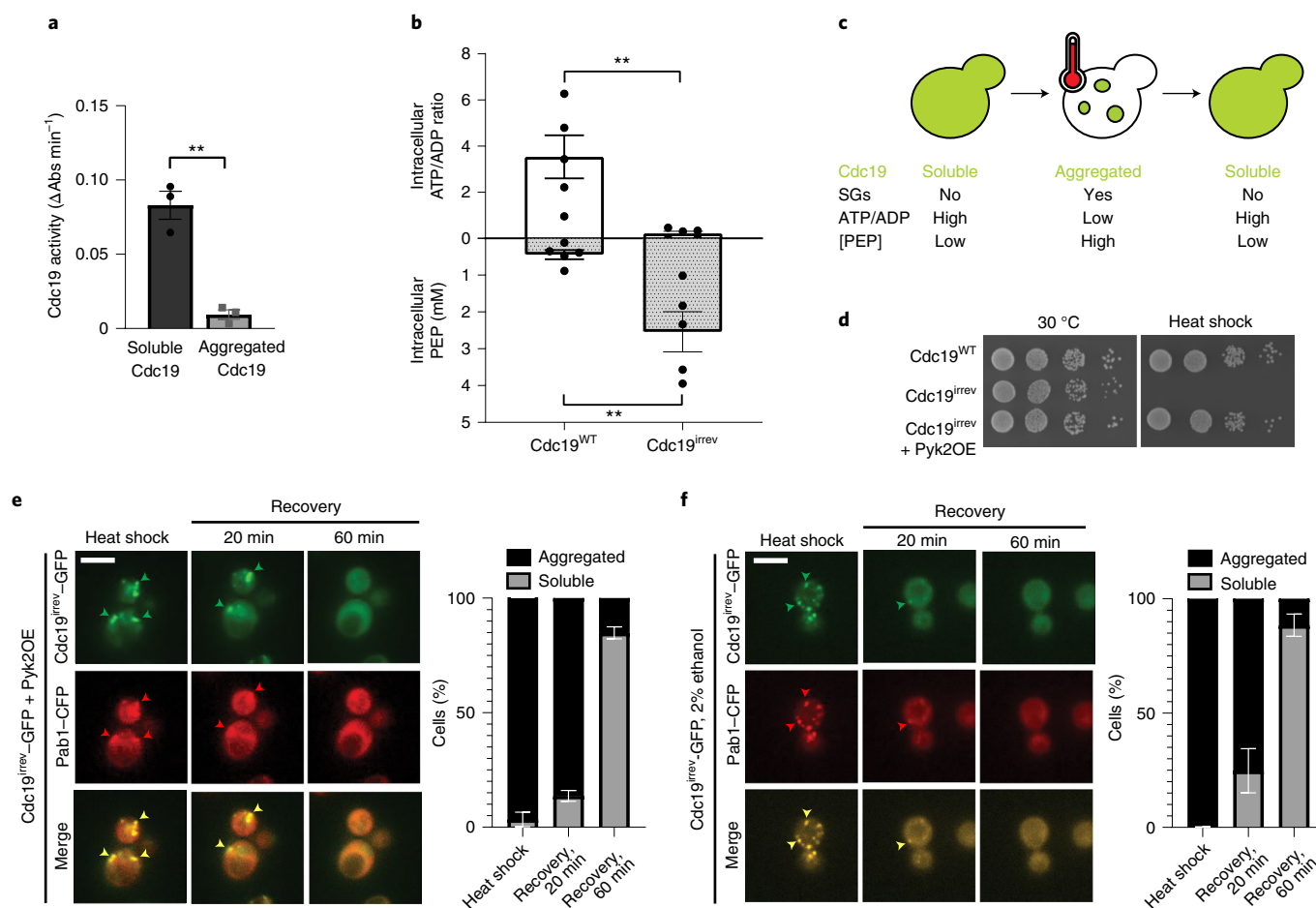
Fig. 1 | SG disassembly depends on the re-solubilization of Cdc19 amyloids. a,b, Cells expressing Cdc19[WT]–GFP (**a**) or Cdc19[irrev]–GFP (**b**) and the SG marker Pab1–cyan fluorescent protein (CFP) were cultured at 30 °C and subjected to heat stress for 30 min at 42 °C before recovery at 30 °C for 60 min. Representative images of the three time points are shown (left). The merged images demonstrate co-localization (arrowheads). The mean ± s.e.m. percentage of cells with Cdc19 aggregates is shown (right; $n = 3$ independent experiments, >30 cells per sample per experiment). Scale bars, 5 μm. **c,d,** Cdc19[WT] (**c**) and Cdc19[irrev] (**d**) proteins purified from *E. coli* were imaged by negative staining TEM. Scale bars, 2 μm. **e,f,** Cdc19[WT] (**e**) and Cdc19[irrev] (**f**) proteins purified from *E. coli* were analysed by circular dichroism spectroscopy before (soluble) or after a 10 min heat shock at 42 °C (aggregated). **c–f,** Representative images of $n = 3$ independent experiments are shown. Source data for all graphical representations are provided.

Results

SG disassembly depends on the re-solubilization of Cdc19 amyloids. The formation of reversible Cdc19 aggregates following stress and their timely re-solubilization after stress release is required to ensure cell survival[4]. Cells expressing an irreversibly aggregating mutant of Cdc19 (Cdc19[irrev]) are unable to restart growth after stress. This Cdc19[irrev] mutant, called Cdc19[4D] in previous work, bears four phosphomimicking mutations in the aggregation-prone Cdc19 LCR (*cdc19-T372D*, *T376D*, *S377D* and *S385D*; Extended Data Fig. 1a). The Cdc19[irrev] protein is active and *cdc19irrev* cells grow similarly to the wild-type in conditions without stress. However following stress, Cdc19[irrev] forms irreversible aggregates and causes persistent SGs (Fig. 1a, b).

To understand how Cdc19 regulates SG disassembly and the mechanisms underlying Cdc19 aggregate re-solubilization, we investigated the properties of wild-type (Cdc19[WT]) and Cdc19[irrev] aggregates as well as potential differences in vitro and in vivo. We examined biophysical characteristics of Cdc19[WT] and Cdc19[irrev] aggregates to understand whether irreversibility was caused by an aberrant aggregate structure. Recombinant Cdc19[WT] and Cdc19[irrev] proteins were produced from *Escherichia coli* and their aggregation was triggered in vitro by heat shock. Both proteins formed needle-like filaments, which were indistinguishable in negative

staining transmission electron microscopy (TEM; Fig. 1c,d). Also in circular dichroism spectroscopy, the wild-type and mutant aggregates revealed similar β-sheet-rich structures (Fig. 1e,f), and both aggregates bound the amyloid dyes Thioflavin T and Congo red[31] (Extended Data Fig. 1b,c), suggesting that Cdc19[WT] and Cdc19[irrev] form similar amyloids in vitro. To test whether the Cdc19 aggregates also exhibit amyloid structures in vivo, we heat shocked and lysed yeast cells and stained both Cdc19[WT] and Cdc19[irrev] aggregates with Congo red. Both cellular Cdc19 aggregates bound the amyloid dye (Extended Data Fig. 1d). Background staining by Congo red is probably due to its ability to also bind cellular structures other than amyloids (for example, cell wall)[32]. To further confirm the amyloid nature of Cdc19 aggregates in vivo, we applied limited proteolysis (LiP) coupled to mass spectrometry (LiP-MS; Extended Data Fig. 1e). This technique allows probing of subtle conformational changes both in vitro and in complex cell lysates and offers more precise structural information compared with conventional methods for detecting amyloids[33,34]. Cdc19 aggregation was induced in vitro by heat shocking purified Cdc19 and in vivo by subjecting cells to starvation stress to achieve full Cdc19 aggregation. The LiP-MS analysis revealed that diagnostic Cdc19 LiP-MS peptides characteristic of the amyloid conformation in vitro resemble the structures observed in vivo. Moreover, conformation-sensitive LiP

Fig. 2 | SG disassembly depends on Cdc19 re-solubilization and restoration of ATP production. a, The activity of purified Cdc19[WT] before (soluble) or after a 30 min heat shock at 42 °C (aggregated) was measured using a lactate dehydrogenase-coupled activity assay as the decrease in absorbance at 340 nm (ΔAbs min^{−1}). The mean ± s.e.m. is indicated (n = 3 independent experiments; two-tailed Student's t-test, **P = 0.0018). **b**, cdc19[irrev] cells are unable to reactivate Cdc19 and resume ATP production after stress release. The intracellular ATP/ADP ratio (top; white bars) and PEP concentration (bottom; shaded bars) were determined in and cdc19[irrev] cells after heat shock at 42 °C for 30 min, followed by recovery at 30 °C for 60 min. The mean ± s.e.m. is shown (n = 5 independent experiments; two-tailed Mann-Whitney tests, both **P = 0.0079). **c**, Schematic showing a yeast cell before (left), during (middle) and after (right) heat stress. During stress, Cdc19 (represented in green) forms inactive aggregates, which co-localize with SGs. Energy levels (ATP/ADP ratio) rapidly decrease under these conditions, whereas PEP accumulates. Following stress release, Cdc19 re-solubilizes, is reactivated and consumes PEP to produce ATP, concomitant with SG disassembly. **d**, Serial dilutions of exponentially growing cells of the indicated genotype were spotted on agar plates before and after heat shock at 42 °C for 30 min and imaged after 3 d at 30 °C (n = 3 independent experiments). **e,f**, ATP production using Cdc19-independent pathways allows Cdc19[irrev] aggregate and SG re-solubilization after stress release. Cells of the indicated genotype were cultured at 30 °C with 2% glucose (**e**) or 2% ethanol (**f**) as the carbon source and subjected to heat stress for 30 min at 42 °C before recovery at 30 °C in the presence of 25 μg ml^{−1} cycloheximide to prevent de novo protein synthesis. Representative images are shown (left) as in Fig. 1a. The mean ± s.e.m. percentage of cells with Cdc19 aggregates (n = 3 independent experiments, >30 cells per sample per experiment) is indicated (right). Scale bars, 5 μm. **d,e**, Pyk2OE, Pyk2 overexpression. Source data for all graphical representations are provided.

peptides were mostly similar in the Cdc19[WT] and Cdc19[irrev] assemblies, suggesting that their different re-solubilization behaviour is not due to radically different structures (Extended Data Fig. 1e). Interestingly, LiP-MS also identified subtle structural alterations in the aggregated catalytic domain of Cdc19. Thus, Cdc19 aggregation and re-solubilization could affect Cdc19 activity and constitute a potential difference between Cdc19[WT] and Cdc19[irrev].

Cdc19 amyloid re-solubilization is crucial for ATP production. The comparison of the enzymatic activity of soluble and aggregated Cdc19 using an established lactate dehydrogenase-coupled pyruvate kinase activity assay revealed that Cdc19 amyloids are enzymatically inactive (Fig. 2a). Given the large conformational changes required for amyloid fibril formation, the loss of catalytic activity is not

surprising. In agreement with this, the cellular energy levels—represented by the ATP/ADP ratio—rapidly dropped in cells exposed to heat stress or glucose starvation, whereas the Cdc19 substrate PEP accumulated under these conditions[14,20–22] (Fig. 2c). Thus, Cdc19 amyloids need to be re-solubilized to reactivate Cdc19 and resume energy production. Given that ATP is essential to disassemble SGs, persistent SGs in cdc19[irrev] cells could be due to impaired ATP production. In contrast to wild-type controls, cdc19[irrev] cells could not metabolise the accumulated PEP and hence failed to restore high ATP levels during stress recovery (Fig. 2b and Extended Data Fig. 1f). We conclude that wild-type and cdc19[irrev] cells differ primarily in their ability to restore energy production after stress.

To test whether an increase in ATP levels was sufficient to disassemble SGs, we restored ATP metabolism in heat-stressed cdc19[irrev]
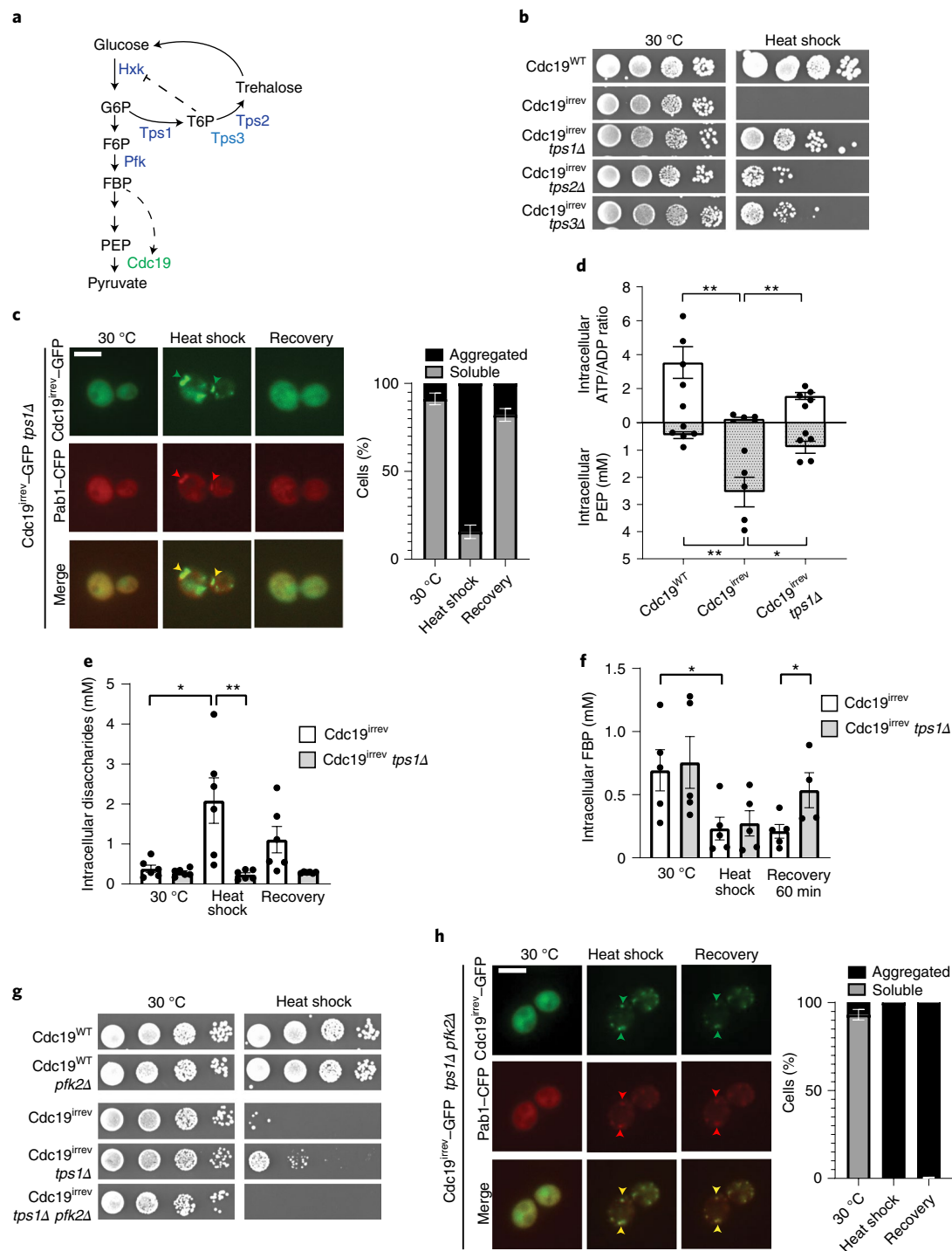
Fig. 3 | Re-solubilization of Cdc19 amyloids and cell-cycle restart after stress are regulated by the glycolytic metabolite FBP. a, Representation of glycolysis and trehalose metabolism. Hxk, hexokinase; and Pfk, phosphofructokinase. **b**, Serial dilutions of the indicated strains were spotted on agar plates before (left) and after heat shock for 30 min at 42 °C (right), and cultured at 30 °C for 3 d (n = 3 independent experiments). **c**, cdc19^{irrev} tps1Δ cells expressing Pab1–CFP were heat shocked for 30 min at 42 °C, and allowed to recover for 90 min at 30 °C. The mean ± s.e.m. percentage of cells with Cdc19 aggregates is shown (right; n = 3 independent experiments, >30 cells per sample per experiment). **d**, The intracellular ATP/ADP ratio (top) and PEP concentration (bottom) were measured in the indicated strains after heat shock for 30 min at 42 °C, and a 60 min recovery at 30 °C. The mean ± s.e.m. is shown (n = 5 independent experiments; two-tailed Mann–Whitney tests, all **P = 0.0079 and *P = 0.0556). **e,f**, Intracellular disaccharides (representing trehalose[46]; **e**) and FBP (**f**) were measured in the indicated strains before, during and 60 min after heat shock (42 °C, 30 min). The mean ± s.e.m. is shown (n = 6 and 5 independent experiments for **e** and **f**, respectively; two-tailed Mann–Whitney tests). **e**, *P = 0.0152 and **P = 0.0022. **f**, both *P = 0.0317. **g**, Serial dilutions of the indicated strains were spotted on agar plates before and after heat shock (42 °C, 30 min) and imaged after 3 d at 30 °C (n = 3 independent experiments). **h**, tps1Δ pfk2Δ cells expressing Pab1–CFP and GFP-tagged Cdc19^{irrev} were heat shocked for 30 min at 42 °C and allowed to recover for 90 min at 30 °C. The intensities of the GFP and CFP signals in the images before heat shock were adjusted for better visualization (left). The mean ± s.e.m. percentage of cells with Cdc19 aggregates is indicated (right; n = 3 independent experiments, >30 cells per sample per experiment). **c,h**, Scale bars, 5 μm. Source data for the graphical representations are provided.

cells by two Cdc19-independent means. First, we artificially overexpressed Pyk2, a pyruvate kinase isoform expressed at low levels in glucose-rich conditions that like Cdc19 uses PEP to produce ATP[35]. Consistent with our hypothesis, Pyk2 overexpression re-solubilized Cdc19[irrev] aggregates and SGs, and restored growth of heat-shocked *cdc19[irrev]* cells (Fig. 2d,e). Second, we cultured *cdc19[irrev]* cells with 2% ethanol instead of glucose. Under these conditions, ATP production occurs mainly via oxidative phosphorylation[36]. This also allowed Cdc19[irrev] aggregate and SG re-solubilization (Fig. 2f). We conclude that under physiological conditions, when yeast cells undergo fermentative growth, re-solubilizing Cdc19 amyloids is critical to resume post-stress ATP production, which is probably required to power ATP-dependent processes critical for SG dissolution and growth restart.

Disassembly of Cdc19 amyloids in vivo is triggered by FBP. To better understand the molecular mechanisms regulating Cdc19 amyloid disassembly, we isolated rare spontaneous suppressors that restore growth of stressed *cdc19[irrev]* cells (Extended Data Fig. 2a). After deleting *PYK2* in the isolated mutants to exclude suppression by upregulated Pyk2 activity, we backcrossed them to wild-type cells to confirm Mendelian segregation of the phenotype. Using whole genome sequencing, we identified a single point mutation in trehalose synthase 3 (Tps3; *tps3-G386D*), a protein involved in trehalose biosynthesis, as the probable cause for the Cdc19[irrev] suppressor phenotype (Extended Data Fig. 2b,c). Trehalose is a disaccharide synthesized in a two-step process (Fig. 3a). Tps1 catalyses the conversion of G6P into trehalose-6-phosphate (T6P), and Tps2 then converts T6P into trehalose. Tps3 acts as cofactor, facilitating trehalose production. Deletion of *TPS1*, *TPS2* or *TPS3* to compromise trehalose synthesis (Extended Data Fig. 2e; ref. [37]) did not alter growth compared with the wild-type (Extended Data Fig. 2d) but allowed *cdc19[irrev]* cells to partially restore growth after stress release (Fig. 3b), suggesting that decreased trehalose metabolism favours Cdc19 re-solubilization. As Tps1 catalyses the first reaction in trehalose synthesis and *TPS1* deletion resulted in the strongest rescue (Fig. 3b), we focussed on this mutant. Fluorescence microscopy confirmed that growth restart correlated with Cdc19[irrev] amyloid re-solubilization and SG disassembly in the *tps1Δ* cells (Fig. 3c). Metabolomic data showed that Cdc19 re-solubilization coincided with restored cellular energy levels after stress. Whereas *cdc19[irrev]* cells failed to increase their ATP/ADP ratio and maintained high intracellular PEP levels after stress, *cdc19[irrev] tps1Δ* cells consumed PEP and increased their ATP/ADP ratio and ATP levels (Fig. 3d). As *TPS1* deletion could also restore growth and Cdc19[irrev] aggregate disassembly in the presence of the respiration inhibitor antimycin A, we conclude that the restoration of energy metabolism depends mainly on reactivation of glycolysis, while oxidative phosphorylation plays

a minor role (Extended Data Fig. 2f,g). Next, we investigated how *TPS1* deletion mediates this rescue. We reasoned that Tps1 activity decreases glycolytic flux by diverting G6P from glycolysis into trehalose synthesis generating T6P, which inhibits hexokinase (Fig. 3a; refs. [27–29]). Thus, *tps1Δ* cells contain virtually no trehalose and have enhanced flux through glycolysis, which results in increased levels of the glycolytic intermediate FBP[29]. The levels of FBP tightly correlate with glycolytic flux and cell growth, with low FBP levels reflecting low glycolysis and stressed, quiescent cells, whereas high FBP levels denote high glycolytic flux and favourable growth conditions[38,39]. Interestingly, besides being a 'glycolytic flux sensor', FBP is also a known allosteric regulator of Cdc19 (ref. [22]). Thus, increased FBP levels in *tps1Δ* cells may directly or indirectly play a role in Cdc19 aggregate disassembly. A comparison of intracellular trehalose and FBP levels in heat-shocked *cdc19[irrev]* and *cdc19[irrev] tps1Δ* cells revealed that a lack of Tps1 abrogated trehalose production (Fig. 3e). Moreover, similar to glucose starvation[29], heat stress induced a rapid decrease in FBP, however during stress recovery, FBP accumulated to significantly higher levels in *cdc19[irrev] tps1Δ* cells compared with the *cdc19[irrev]* controls (Fig. 3f). To genetically test whether increased FBP levels mediate the observed rescue of stressed *cdc19[irrev]* cells by *tps1Δ*, we impaired FBP production by deleting Pfk2 (*pfk2Δ*), the main FBP-producing enzyme[29]. In contrast to the *cdc19[irrev] tps1Δ* cells, the *cdc19[irrev] tps1Δ pfk2Δ* mutants were unable to recover from heat stress, whereas *pfk2Δ* alone neither significantly reduced the growth rates nor impaired survival to stress (Fig. 3g). Moreover, the *cdc19[irrev] tps1Δ pfk2Δ* cells were also unable to dissolve Cdc19[irrev] aggregates and SGs (Fig. 3h). Importantly, the levels of Cdc19 were not altered in any of the mutants (Extended Data Fig. 2h). We conclude that high FBP levels contribute to efficient stress recovery, and Cdc19 amyloid and SG disassembly.

Altered trehalose levels might also influence Cdc19 re-solubilization by other means, as trehalose affects SG dynamics by tuning the cytoplasmic viscosity[40]. Deletion of *TPS2* also rescued the aggregate dissolution defects observed in the *cdc19[irrev]* cells (Extended Data Fig. 2i), although this effect was weaker compared with *tps1Δ* cells (Fig. 3b). Although both strains were impaired in trehalose synthesis, only the deletion of *TPS1* (and not *TPS2*) resulted in increased post-stress FBP levels in the *cdc19* cells (Extended Data Fig. 2j). We conclude that FBP-dependent and -independent mechanisms cooperate to achieve efficient Cdc19 amyloid disassembly after stress, but increased cytoplasmic viscosity via trehalose breakdown plays a minor role compared with increased FBP levels.

FBP binding regulates Cdc19 amyloid assembly and disassembly. Mechanistically, direct binding of FBP to Cdc19 could reduce aggregation by promoting Cdc19 tetramerization (Fig. 4a(i)),

Fig. 4 | FBP directly regulates the formation and disassembly of reversible Cdc19 amyloids. a, Illustration of how FBP binding may regulate Cdc19 amyloid formation and disassembly. FBP depletes aggregation-prone monomers by inducing Cdc19 tetramerization[4] (i) and directly promotes aggregate re-solubilization (ii). **b–d**, Purified Cdc19[WT] (**b**), Cdc19[ΔFBP] (**c**) and Cdc19[irrev] (**d**) proteins were mixed with the indicated metabolites and incubated at 30 °C for 14 h. After centrifugation, the supernatant (Sup) and pellet fractions were analysed by SDS–PAGE (left) and quantified relative to the buffer controls (middle and right; shown as the mean ± s.e.m.; n = 3 independent experiments; two-tailed Student's t-test, *P = 0.0342). **e,f**, Cdc19[irrev] is monomeric in vivo and in vitro. **e**, Extracts from cells expressing GFP-tagged Cdc19[WT] or Cdc19[irrev] were separated by size-exclusion chromatography and selected peak fractions were analysed by western blotting with an antibody to GFP (α-GFP). **f**, Recombinant Cdc19[WT], Cdc19[irrev] and Cdc19[ΔPEP] mutant (as a control tetramer) proteins were purified and analysed by size-exclusion chromatography. The normalized absorbance at 215 nm was plotted as a function of the elution volume; n = 3 independent experiments. **g**, Direct FBP binding to Cdc19 is necessary to re-solubilize Cdc19 amyloids in vivo. Wild-type and *tps1Δ* cells expressing GFP-tagged Cdc19[WT] or Cdc19[ΔFBP] and overexpressing Pyk2 were heat shocked (42 °C, 30 min; left) and allowed to recover at 30 °C in the presence of 25 µg ml⁻¹ cycloheximide. Representative GFP images (n = 3 independent experiments) were taken 60 (middle) or 240 min (right) after the heat shock. The arrowheads indicate Cdc19–GFP aggregates. Scale bars, 5 µm. **h**, Heat shock-induced (42 °C, 10 min) Cdc19[WT] (top), Cdc19[ΔFBP] (middle) and Cdc19[irrev] (bottom) amyloids were incubated with FBP (4 or 8 mM) or for control F6P (4 mM) or buffer. Scale bars, 500 nm. The black arrowheads mark fibrils that became positively stained due to FBP binding. Representative fibrils (dashed squares) were enlarged ×1.5 for better visualization of the distinct fibril morphologies (insets); n = 3 independent experiments. Unprocessed original scans of gels and blots as well as the source data for all graphical representations are provided; a.u., arbitrary units.

as Cdc19 tetramers are less aggregation-prone than monomers[4]. Alternatively, FBP could directly bind to Cdc19 amyloids and facilitate Cdc19 aggregate and SG disassembly (Fig. 4a(ii)). These two action modes are not mutually exclusive and could cooperate to ensure rapid Cdc19 re-solubilization. A centrifugation assay revealed that incubation of purified Cdc19[WT] with 5 mM FBP, but
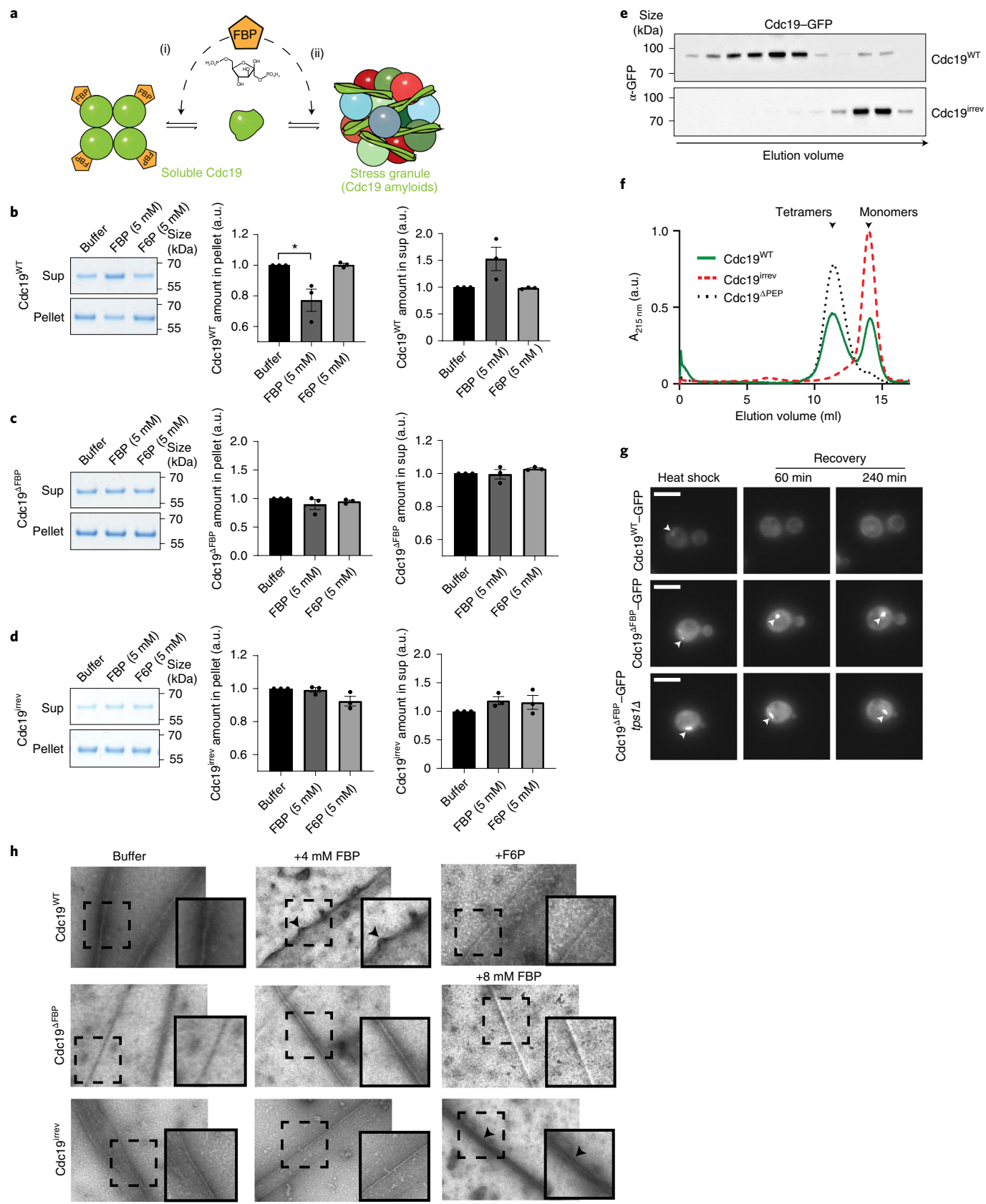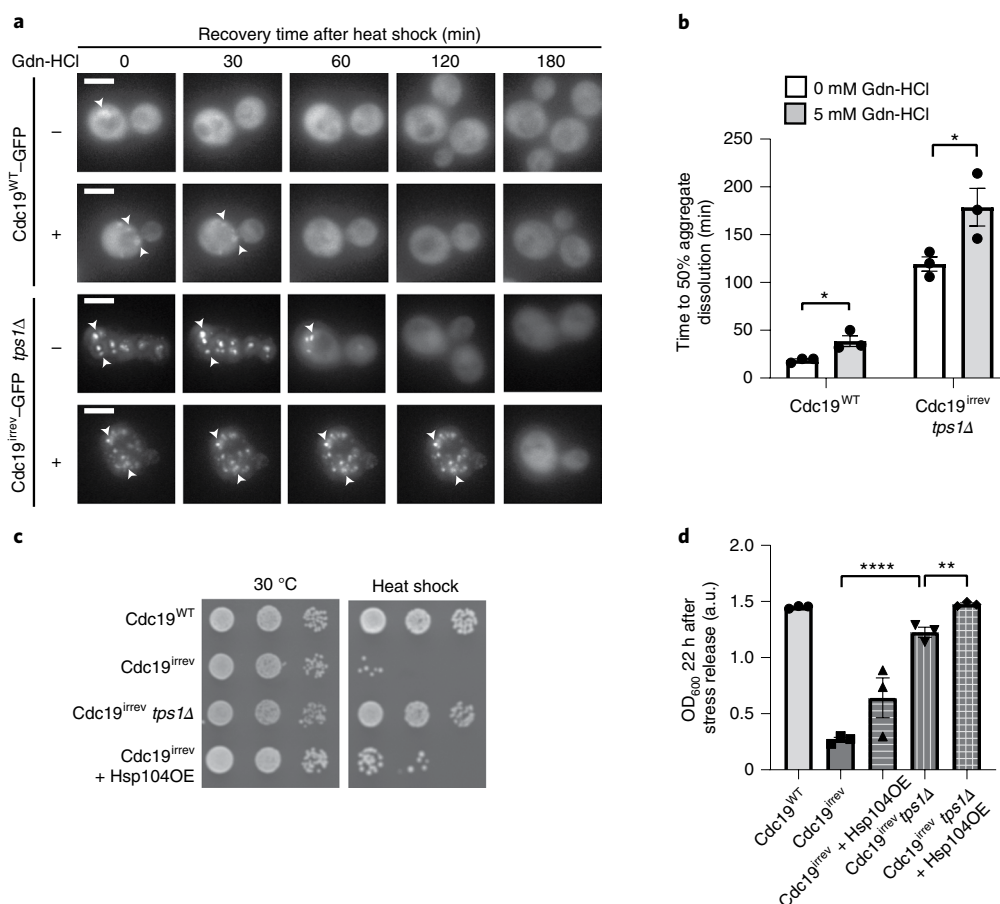
Fig. 5 | Chaperones are involved in Cdc19 amyloid disassembly. a,b, Inhibition of Hsp104 activity delays Cdc19 and SG re-solubilization. Cells of the indicated genotype were treated with 5 mM Gdn-HCl for 3 h, followed by heat shock (42 °C, 30 min). **a,** The aggregate disassembly after stress release was monitored by fluorescence microscopy. Representative images; the arrowheads indicate Cdc19 aggregates ($n = 3$ independent experiments). Scale bars, 5 μm. **b,** Cdc19 aggregate disassembly was quantified by counting the number of foci at different time points after stress. The average time to 50% aggregate dissolution ± s.e.m. is displayed ($n = 3$ independent experiments, >30 cells per sample per experiment; two-tailed Student's t-test, Cdc19^{WT}, *$P = 0.0268$ and Cdc19^{irrev} $tps1\Delta$, *$P = 0.048$). **c,d,** Overexpression of Hsp104 partially rescues growth of $cdc19^{irrev}$ cells after heat shock. **c,** Serial dilutions of exponentially growing cells of the indicated genotype were spotted on agar plates before (left) and after a 42 °C heat shock for 30 min, and imaged after 3 d at 30 °C ($n = 3$ independent experiments). Overexpression of Hsp104 (Hsp104OE) was induced by treating cells with 10 mM estradiol for 3 h (bottom row). **d,** Growth restart was also quantified by measuring the cell density (OD$_{600}$) over time after inoculation of equal cell numbers at 30 °C. The mean OD$_{600}$ ± s.e.m. is shown ($n = 3$ independent experiments; two-tailed Student's t-tests, ****$P = 0.0000413$ and **$P = 0.0055$); a.u., arbitrary units. Source data for all graphical representations are provided.

not with its structurally related precursor fructose-6-phosphate (F6P), interfered with aggregate formation (Fig. 4b). In the presence of FBP, a significant portion of Cdc19^{WT} indeed remained soluble, with a corresponding decrease in the aggregated pellet fraction. Conversely, the addition of 5 mM ATP, PEP or trehalose did not influence Cdc19 aggregation (Extended Data Fig. 3a–c). To confirm that FBP reduces Cdc19 aggregation by direct binding, we measured the aggregation behaviour of a Cdc19 point mutant ($cdc19$-$T403E$) that is unable to bind FBP (Cdc19$^{\Delta FBP}$)[41]. Addition of FBP did not interfere with heat shock-induced Cdc19$^{\Delta FBP}$ aggregation (Fig. 4c). Thus, direct FBP binding to Cdc19 monomers partially prevents amyloid formation by promoting the formation of Cdc19 tetramers (Fig. 4a(i)). However, FBP did not affect Cdc19^{irrev} aggregate formation (Fig. 4d), suggesting that this mutant might have a reduced ability to bind FBP and/or to tetramerize. Size-exclusion chromatography demonstrated that Cdc19^{irrev} is fully monomeric both in vivo and in vitro (Fig. 4e,f). These results imply that the FBP-mediated rescue of Cdc19^{irrev} in vivo cannot simply be explained by increased tetramerization (Fig. 4a(i)), but FBP must also promote aggregate disassembly (Fig. 4a(ii)). To confirm that direct FBP binding to

Cdc19 amyloids is required for their disassembly, we compared the aggregation dynamics of Cdc19^{WT} and Cdc19$^{\Delta FBP}$ in vivo (Fig. 4g). Interestingly, Cdc19$^{\Delta FBP}$ was soluble under favourable growth conditions but rapidly formed irreversible aggregates following heat shock, which could not be disassembled after stress recovery. In contrast to Cdc19^{irrev}, the Cdc19$^{\Delta FBP}$ aggregates could not be rescued by increasing the FBP levels through $TPS1$ deletion, implying that direct FBP binding to Cdc19 is essential to disassemble Cdc19 amyloids in vivo.

Next, we examined whether FBP is sufficient to disassemble pre-formed Cdc19 amyloids in vitro. We induced fibril formation of purified Cdc19^{WT} by heat shock and incubated the obtained amyloids with varying FBP concentrations. Analysis by SDS-PAGE of the soluble and insoluble fractions after centrifugation revealed no noticeable Cdc19 re-solubilization even upon incubation with FBP in excess (20 mM), thereby indicating that FBP binding is not sufficient to disassemble Cdc19 amyloids in vitro (Extended Data Fig. 3d). However, FBP bound directly to Cdc19 amyloids and altered their appearance in negative staining TEM. Incubation of pre-formed Cdc19^{WT} aggregates with FBP (4 mM) resulted in

fibrils that were consistently positively stained (of dark colour; Fig. 4h, +FBP) in contrast to the negatively stained fibrils (white) in the absence of FBP. This change from negative (white fibrils) to positive (black fibrils) staining results from acidic FBP molecules bound to fibrils attracting the positively charged uranyl stain. In contrast, incubation of pre-formed Cdc19^{WT} amyloids with buffer (Fig. 4h, buffer) or F6P (Fig. 4h, +F6P) did not cause any visible changes, so the Cdc19^{WT} amyloids appeared as negatively stained, needle-like fibrils characterized by smooth edges. Cdc19$^{\Delta FBP}$ amyloid fibrils incubated with FBP also retained their straight, smooth morphology with negative staining even at high concentrations of FBP (8 mM), validating that the observed alterations are induced by direct FBP binding to Cdc19 (Fig. 4h, lower panels). Interestingly, Cdc19^{irrev} showed intermediate signs of fibril curvature, uneven borders and positive staining compared with Cdc19^{WT} and Cdc19$^{\Delta FBP}$, and these changes were apparent only at high FBP concentrations (8 mM), confirming reduced FBP binding by Cdc19^{irrev}. We conclude that although FBP directly binds to Cdc19 fibrils, binding is not sufficient to trigger Cdc19 amyloid re-solubilization in vitro. However, FBP may facilitate morphological changes and/or factor recruitment that promotes efficient amyloid disassembly observed in vivo.

Chaperones contribute to Cdc19 amyloid re-solubilization. Chaperones such as Hsp104 and Ssa2 have been implicated in remodelling protein assemblies and SGs, and cells lacking *HSP104* or *SSA1/2* are slightly delayed in SG disassembly[17,42,43]. Thus, we tested whether these chaperones are also involved in Cdc19 disaggregation. We observed that Gdn-HCl-mediated inhibition of Hsp104 activity delayed dissolution of both Cdc19^{WT} and Cdc19^{irrev} aggregates in *tps1Δ* cells (Fig. 5a,b). Conversely, overexpression of Hsp104 was sufficient to partially restore growth of heat-stressed *cdc19^{irrev}* cells (Fig. 5c), which was further enhanced by a simultaneous increase in Ssa2 levels (Extended Data Fig. 4a,b). Moreover, Hsp104 overexpression slightly improved the growth of *cdc19^{irrev} tps1Δ* mutants after heat stress, indicating that increased FBP and chaperone levels have an additive effect (Fig. 5d). Increasing the FBP levels by *TPS1* deletion allowed rapid growth restart after stress, whereas Hsp104 overexpression seemed to facilitate growth in a later phase, suggesting that high FBP may be particularly important in the initial steps of Cdc19 amyloid disassembly (Extended Data Fig. 4c). Together, these results imply that FBP binding to Cdc19 initiates aggregate re-solubilization and cooperates with Hsp104 and Ssa2 to disassemble SG in vivo.

FBP binding to Cdc19 amyloids promotes chaperone recruitment. Next, we compared the localization of Cdc19, tagged with green fluorescent protein (GFP), and Hsp104–mCherry or Ssa2–mCherry in wild-type, *cdc19^{irrev}* and *cdc19^{irrev} tps1Δ* cells. Fluorescence microscopy confirmed that Hsp104–mCherry and Ssa2–mCherry co-localized with heat shock-induced Cdc19–GFP aggregates in the majority of wild-type cells (Fig. 6a,b). However, Hsp104 and Ssa2 were surprisingly not recruited to irreversible Cdc19^{irrev} aggregates but remained dispersed throughout the cytoplasm. Co-localization was restored following *TPS1* deletion, consistent with the idea that increased FBP levels and FBP binding to Cdc19 allow chaperone recruitment to SGs (Fig. 6a,b) to promote Cdc19 and SG re-solubilization (Extended Data Fig. 4d). To corroborate these results, we examined the co-localization of Hsp104–mCherry with GFP-tagged Cdc19$^{\Delta FBP}$. As expected, the Cdc19$^{\Delta FBP}$ amyloids failed to recruit Hsp104–mCherry and co-localization could not be restored by *TPS1* deletion, confirming that FBP binding to Cdc19 is essential for chaperone recruitment (Fig. 6c). In this background, Hsp104–mCherry showed a punctate pattern by binding to heat-induced aggregates, but these foci did not co-localize with irreversible Cdc19$^{\Delta FBP}$ amyloids (Fig. 6c). We thus conclude that FBP binding to Cdc19 aggregates promotes chaperone binding and allows their recruitment to SGs, which is essential for Cdc19 amyloid re-solubilization, restoration of ATP production and SG disassembly.

Discussion

Cell survival under stress conditions requires rapid and reversible implementation of protective measures, including the timely formation and disassembly of reversible aggregates and SGs. Here we show that during stress, the essential ATP-producing enzyme Cdc19 forms proteolysis-resistant reversible amyloids which co-localize with SGs. Aggregation not only protects Cdc19 from stress-induced degradation but also inactivates the enzyme, leading to a rapid decrease of cellular ATP. However, ATP is required for post-stress Cdc19 aggregate and SG disassembly as well as growth restart[14]. We show that Cdc19 amyloid re-solubilization after stress restores the cellular energy levels and that this is essential to disassemble SGs and restart growth. Moreover, our results unravel a multi-step mechanism for Cdc19 amyloid and SG re-solubilization. The glycolytic metabolite FBP regulates the assembly state and activity of Cdc19 in two ways (Fig. 6d). First, during exponential growth, FBP binds to soluble Cdc19, promoting the formation of active non-aggregating Cdc19 tetramers. During stress, decreasing FBP levels facilitate the formation of aggregation-prone Cdc19 monomers, which assemble into amyloid structures. Second, following stress release, glycolysis restarts and increasing FBP levels trigger Cdc19 re-solubilization. FBP directly binds to Cdc19 amyloids and promotes efficient recruitment of Hsp104 and Ssa2 chaperones. A dedicated algorithm[44] predicts a specific binding site for Hsp70 chaperones co-localizing with the FBP-binding site

Fig. 6 | FBP binding to Cdc19 amyloids promotes chaperone recruitment, triggering Cdc19 re-solubilization and SG disassembly in vivo. a–c, Binding of FBP to Cdc19 amyloids promotes chaperone recruitment, which correlates with aggregate disassembly. Wild-type and *tps1Δ* cells co-expressing mCherry-tagged Hsp104 (**a,c**) or Ssa2 (**b**) and either GFP-tagged Cdc19^{WT}, Cdc19^{irrev} or Cdc19$^{\Delta FBP}$ were subjected to heat stress for 30 min at 42 °C and imaged by fluorescence microscopy. Representative GFP and mCherry images are shown together with the merged image to visualize the co-localization of Cdc19 aggregates and the chaperones (top; *n* = 3 independent experiments). Scale bars, 5 μm. The mean ± s.e.m. percentage of cells with co-localized Cdc19 and Hsp104 (**a,c**) or Ssa2 (**b**) foci are shown (*n* = 3 independent experiments, >300 cells per sample per experiment). **c**, *cdc19$^{\Delta FBP}$* cells overexpress Pyk2 to restore ATP production and cell viability. **d**, Molecular network coupling cellular metabolism with reversible Cdc19 amyloids and SG dynamics. During cell growth, the metabolite FBP is produced through glycolysis and its binding to Cdc19 promotes the formation of active non-aggregation-prone Cdc19 tetramers. During stress, the FBP levels drop rapidly, leading to tetramer disassembly and the accumulation of Cdc19 monomers. In this state, Cdc19 exposes its aggregation-prone LCR and is primed to form Cdc19 amyloids, which are inactive and accumulate in SGs. After stress release, the FBP levels rise and FBP directly binds to Cdc19 amyloids, thereby facilitating the recruitment of Hsp104 and Ssa2 to the aggregates. These chaperones allow re-solubilization of Cdc19 amyloids and the release of Cdc19 monomers. Re-solubilized, active Cdc19 in turn uses PEP to produce ATP, which is required to activate chaperones to further solubilize Cdc19 and increase energy production. This positive feedback loop fuels the disassembly of Cdc19 amyloids and other SG components. Concomitant breakdown of trehalose liberates glucose moieties for glycolysis and modulates cytoplasmic diffusion. Orchestrated disassembly of SGs then releases several mRNAs and metabolic enzymes, and allows full resumption of cell growth and cell-cycle progression. Source data for all graphical representations are provided.

of Cdc19. Cells expressing a Cdc19$^{\Delta FBP}$ mutant, which cannot bind FBP, fail to recruit chaperones and cannot disassemble Cdc19 aggregates after stress release. Moreover, FBP further increases the ATP production by Cdc19, facilitating chaperone recruitment and activity. Re-solubilized Cdc19 produces ATP, which further fuels Cdc19 amyloid and SG disassembly in a positive feedback loop. Although Hsp104 was identified as the critical ATP-consuming enzyme during this process[14], other cellular factors such as RNA/DNA-helicases, protein kinases and AAA-ATPases may also contribute to dissolve SGs and restart cell growth[9]. In summary, FBP functions as a

'glycolytic flux sensor'[38,39] and directly controls Cdc19 amyloid formation and disassembly. The need for ATP production by Cdc19 can be bypassed with non-glycolytic substrates, which are metabolised by oxidative phosphorylation in mitochondria.

Conceptually, our results reveal a mechanism whereby the metabolic and energetic state of the cell is coupled to SG disassembly via the regulated formation of Cdc19 amyloids. We uncovered a crucial function of reversible Cdc19 amyloids in SG regulation and cell survival under stress, highlight Cdc19 amyloids as physiological targets of Hsp104 and Ssa2, and elucidate how functional
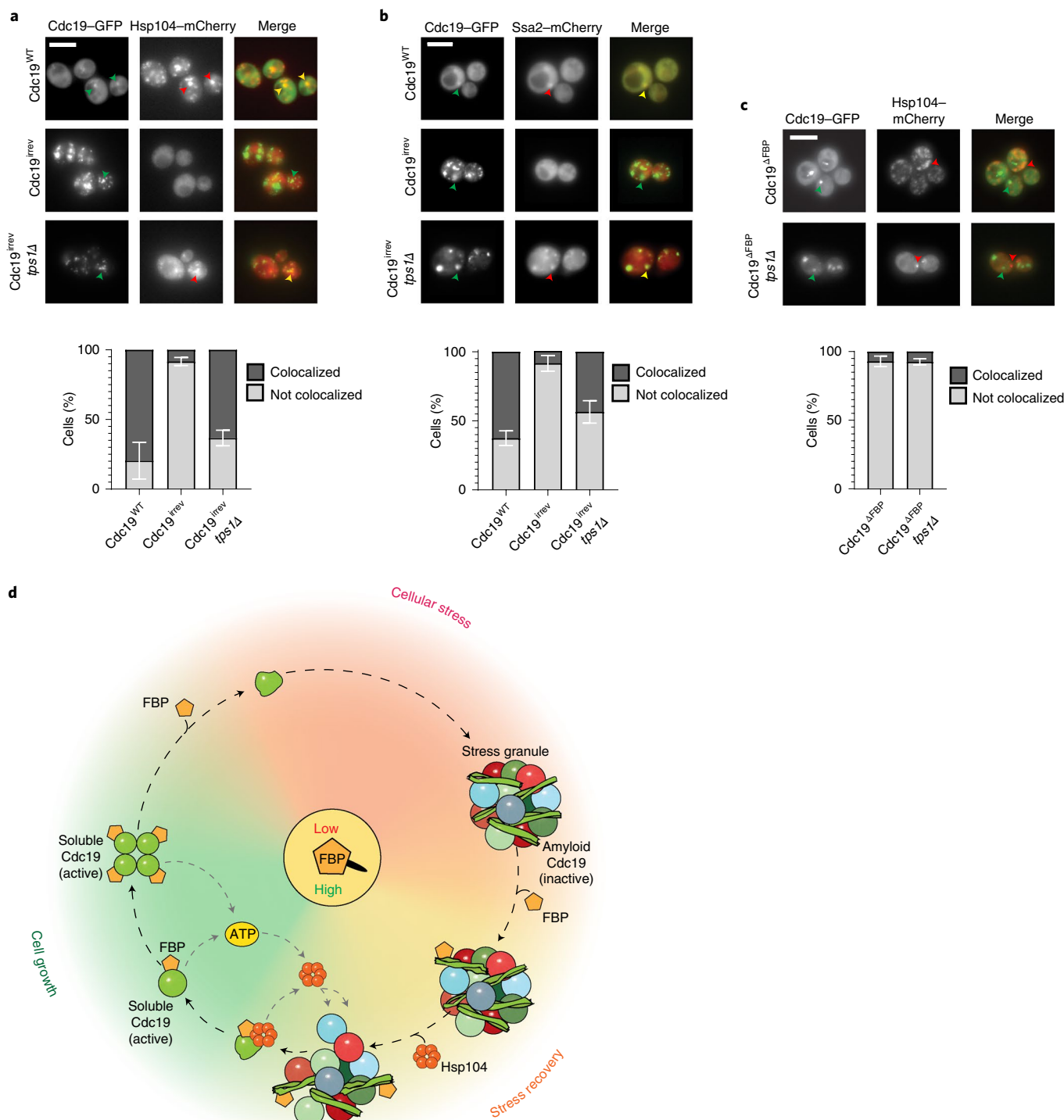
amyloids can be disassembled in a physiological context. As several metabolic enzymes reversibly aggregate during stress[45], similar mechanisms may regulate their activity. Finally, although the interplay between physiological and pathological amyloids remains to be explored, understanding the regulation of physiological amyloids might provide important insights into the pathogenesis of neurodegenerative diseases.

Online content

Any methods, additional references, Nature Research reporting summaries, source data, extended data, supplementary information, acknowledgements, peer review information; details of author contributions and competing interests; and statements of data and code availability are available at https://doi.org/10.1038/s41556-021-00760-4.

References

1. Fulda, S. et al. Cellular stress responses: cell survival and cell death. *Int. J. Cell Biol.* **2010**, 214074 (2010).
2. Aulas, A. et al. Stress-specific differences in assembly and composition of stress granules and related foci. *J. Cell Sci.* **130**, 927–937 (2017).
3. Protter, D. S. W. & Parker, R. Principles and properties of stress granules. *Trends Cell Biol.* **26**, 668–679 (2016).
4. Saad, S. et al. Reversible protein aggregation is a protective mechanism to ensure cell cycle restart after stress. *Nat. Cell Biol.* **19**, 1202–1213 (2017).
5. Begovich, K. et al. Conserved metabolite regulation of stress granule assembly via AdoMet. *J. Cell Biol.* **219**, e201904141 (2020).
6. Cabrera, M. et al. Chaperone-facilitated aggregation of thermo-sensitive proteins shields them from degradation during heat stress. *Cell Rep.* **30**, 2430–2443 (2020).
7. Wolozin, B. & Ivanov, P. Stress granules and neurodegeneration. *Nat. Rev. Neurosci.* **20**, 649–666 (2019).
8. Cao, X., Jin, X. & Liu, B. The involvement of stress granules in aging and aging-associated diseases. *Aging Cell* **19**, e13136 (2020).
9. Jain, S. et al. ATPase-modulated stress granules contain a diverse proteome and substructure. *Cell* **164**, 487–498 (2016).
10. Molliex, A. et al. Phase separation by low complexity domains promotes stress granule assembly and drives pathological fibrillization. *Cell* **163**, 123–133 (2015).
11. Banani, S. F. et al. Biomolecular condensates: organizers of cellular biochemistry. *Nat. Rev. Mol. Cell Biol.* **18**, 285–298 (2017).
12. Van Treeck, B. et al. RNA self-assembly contributes to stress granule formation and defining the stress granule transcriptome. *Proc. Natl Acad. Sci. USA* **115**, 2734–2739 (2018).
13. Kroschwald, S. et al. Different material states of Pub1 condensates define distinct modes of stress adaptation and recovery. *Cell Rep.* **23**, 3327–3339 (2018).
14. Sathyanarayanan, U. et al. ATP hydrolysis by yeast Hsp104 determines protein aggregate dissolution and size in vivo. *Nat. Commun.* **11**, 5226 (2020).
15. Shattuck, J. E. et al. The prion-like protein kinase Sky1 is required for efficient stress granule disassembly. *Nat. Commun.* **10**, 3614 (2019).
16. Wang, B. et al. ULK1 and ULK2 regulate stress granule disassembly through phosphorylation and activation of VCP/p97. *Mol. Cell* **74**, 742–757 (2019).
17. Walters, R. W. et al. Differential effects of Ydj1 and Sis1 on Hsp70-mediated clearance of stress granules in *Saccharomyces cerevisiae*. *RNA* **21**, 1660–1671 (2015).
18. Patel, A. et al. ATP as a biological hydrotrope. *Science* **356**, 753–756 (2017).
19. Hofmann, S. et al. Translation suppression promotes stress granule formation and cell survival in response to cold shock. *Mol. Biol. Cell* **23**, 3786–3800 (2012).
20. Weitzel, G., Pilatus, U. & Rensing, L. The cytoplasmic pH, ATP content and total protein synthesis rate during heat-shock protein inducing treatments in yeast. *Exp. Cell. Res.* **170**, 64–79 (1987).
21. Soini, J. et al. Transient increase of ATP as a response to temperature up-shift in *Escherichia coli*. *Micro. Cell Fact.* **4**, 9 (2005).
22. Xu, Y. F. et al. Regulation of yeast pyruvate kinase by ultrasensitive allostery independent of phosphorylation. *Mol. Cell* **48**, 52–62 (2012).
23. Fiechter, A., Fuhrmann, G. F. & Käppeli, O. Regulation of glucose metabolism in growing yeast cells. *Adv. Micro. Physiol.* **22**, 123–183 (1981).
24. Flores, C. L. et al. Carbohydrate and energy-yielding metabolism in non-conventional yeasts. *FEMS Microbiol. Rev.* **24**, 507–529 (2000).
25. Grignaschi, E. et al. A hydrophobic low-complexity region regulates aggregation of the yeast pyruvate kinase Cdc19 into amyloid-like aggregates in vitro. *J. Biol. Chem.* **293**, 11424–11432 (2018).
26. Anastasiou, D. et al. Pyruvate kinase M2 activators promote tetramer formation and suppress tumorigenesis. *Nat. Chem. Biol.* **8**, 839–847 (2012).
27. Blázquez, M. A. et al. Trehalose-6-phosphate, a new regulator of yeast glycolysis that inhibits hexokinases. *FEBS Lett.* **329**, 51–54 (1993).
28. van Vaeck, C. et al. Analysis and modification of trehalose 6-phosphate levels in the yeast *Saccharomyces cerevisiae* with the use of *Bacillus subtilis* phosphotrehalase. *Biochem. J.* **353**, 157–162 (2001).
29. Peeters, K. et al. Fructose-1,6-bisphosphate couples glycolytic flux to activation of Ras. *Nat. Commun.* **8**, 922 (2017).
30. Cereghetti, G. et al. Reversible, functional amyloids: towards an understanding of their regulation in yeast and humans. *Cell Cycle* **17**, 1545–1558 (2018).
31. Villar-Piqué, A. et al. Screening for amyloid aggregation: in-silico, in-vitro and in-vivo detection. *Curr. Protein Pept. Sci.* **15**, 477–489 (2014).
32. Linder, T. Evaluation of the chitin-binding dye Congo red as a selection agent for the isolation, classification, and enumeration of ascomycete yeasts. *Arch. Microbiol.* **200**, 671–675 (2018).
33. Feng, Y. et al. Global analysis of protein structural changes in complex proteomes. *Nat. Biotechnol.* **32**, 1036–1044 (2014).
34. Cappelletti, V. et al. Dynamic 3D proteomes reveal protein functional alterations at high resolution in situ. *Cell* **184**, 545–559 (2021).
35. Boles, E. et al. Characterization of a glucose-repressed pyruvate kinase (Pyk2p) in *Saccharomyces cerevisiae* that is catalytically insensitive to fructose-1,6-bisphosphate. *J. Bacteriol.* **179**, 2987–2993 (1997).
36. Orlandi, I. et al. Ethanol and acetate acting as carbon/energy sources negatively affect yeast chronological aging. *Oxid. Med. Cell. Longev.* **2013**, 802870 (2013).
37. Bell, W. et al. Composition and functional analysis of the *Saccharomyces cerevisiae* trehalose synthase complex. *J. Biol. Chem.* **273**, 33311–33319 (1998).
38. Monteiro, F. et al. Measuring glycolytic flux in single yeast cells with an orthogonal synthetic biosensor. *Mol. Syst. Biol.* **15**, e9071 (2019).
39. Ji, F. et al. Determination of intracellular metabolites concentrations in *Escherichia coli* under nutrition stress using liquid chromatography-tandem mass spectrometry. *Talanta* **189**, 1–7 (2018).
40. Persson, L.B., Ambati, V.S. & Brandman, O. Cellular control of viscosity counters changes in temperature and energy availability. *Cell* **183**, 1572–1585 (2020).
41. Fenton, A. W. & Blair, J. B. Kinetic and allosteric consequences of mutations in the subunit and domain interfaces and the allosteric site of yeast pyruvate kinase. *Arch. Biochem. Biophys.* **397**, 28–39 (2002).
42. Cherkasov, V. et al. Coordination of translational control and protein homeostasis during severe heat stress. *Curr. Biol.* **23**, 2452–2462 (2013).
43. Mogk, A., Bukau, B. & Kampinga, H. H. Cellular handling of protein aggregates by disaggregation machines. *Mol. Cell* **69**, 214–226 (2018).
44. Gutierres, M. B. B., Bonorino, C. B. C. & Rigo, M. M. ChaperISM: improved chaperone binding prediction using position-independent scoring matrices. *Bioinformatics* **36**, 735–741 (2020).
45. Narayanaswamy, R. et al. Widespread reorganization of metabolic enzymes into reversible assemblies upon nutrient starvation. *Proc. Natl Acad. Sci. USA* **106**, 10147–10152 (2009).
46. Plata, M. R. et al. Determination of carbohydrates present in *Saccharomyces cerevisiae* using mid-infrared spectroscopy and partial least squares regression. *Anal. Bioanal. Chem.* **405**, 8241–8250 (2013).

Methods

Media, growth assays, yeast strains and plasmid construction. The yeast strains and plasmids used in this work were obtained using standard molecular biology protocols and are listed in Supplementary Tables 1 and 2, respectively. Unless otherwise stated, yeast cells were cultured at 30 °C in synthetic defined (SD) medium with 2% glucose (2% glucose, 0.5% NH$_4$-sulfate, 0.17% yeast nitrogen base and amino acids), as previously described[4]. Where indicated, the 2% glucose in the SD medium was substituted with 2% ethanol. When grown exponentially, $cdc19^{irrev}$ strains were never allowed to grow above an optical density at 600 nm (OD$_{600}$) of 0.8 to avoid stress conditions. Heat shock was induced by moving exponentially growing cells (OD$_{600}$ 0.4–0.6) to 42 °C for 30 min. Where indicated, cycloheximide (Sigma-Aldrich, C-7698) or antimycin A (Sigma-Aldrich, A8674) was added to the medium at a final concentration of 25 µg ml^{-1} or 2 µM (1 µM in SD plates), respectively. Hsp104 activity was inhibited with 5 mM Gdn-HCl (Sigma-Aldrich, 50950) for 3 h before stress initiation. Growth rates at 30 °C were determined by measuring the OD$_{600}$ in a 96-well plate (Greiner Bio-One) using a plate reader (BioLector m2p-labs or ClarioStar BMG Labtech) or by imaging serial dilution spottings onto the appropriate SD plates after 3 d. Protein overexpression from estradiol-inducible promoters was achieved by exposing cells to 10 mM estradiol (Sigma-Aldrich, E8875) for 3 h.

Fluorescence microscopy, image analysis and quantification. Fluorescence microscopy was performed using a Nikon Eclipse Ti-E microscope with the MicroManager v. 1.4 and NIS-Elements Advanced Research v. 5.02 software. For the time-lapse experiments, cells were loaded in microfluidic plates (CellASIC ONIX2, Merck Millipore) at 30 °C[4]. Heat shock was induced with the microfluidic plate temperature controller by increasing the temperature to 42 °C for 30 min before returning it to 30 °C or by moving the cultures to a pre-heated shaking incubator (Kühner, LT W Lab-Therm) at 42 °C for 30 min. Images were recorded every 10 min and quantified as described in the figure legends.

Screen for suppressors of irreversible Cdc19 aggregates. Cells expressing Cdc19^{irrev}–GFP were cultured in SD-His medium (SD medium lacking His) to an OD$_{600}$ of 0.6, heat shocked for 30 min at 42 °C in a shaking incubator (Kühner, LT W Lab-Therm), collected by centrifugation and spread on SD-His plates to single colonies. Individual colonies that survived were isolated and visually inspected by fluorescence microscopy. *PYK2* was deleted by homologous recombination to exclude suppressors that upregulate Pyk2. The suppressors were backcrossed to ensure Mendelian segregation and suppressor strains with single gene traits were subjected to whole genome sequencing. The identified mutations were validated by crossing *cdc19^{irrev}* strains with full deletions of the mutated gene.

Protein purification. Plasmids expressing wild-type or mutant Cdc19-Strep (Cdc19 fused to a C-terminal Strep-tag) constructs were transformed into *E. coli* cells (Rosetta). The cells were cultured at 37 °C in LB medium (1% peptone, 0.5% yeast extract and 0.5% NaCl), with 30 µg ml^{-1} chloramphenicol and 100 µg ml^{-1} carbenicillin, to an OD$_{600}$ of 0.6. Protein production was induced by adding 0.1 mM isopropyl-β-D-thiogalactoside (IPTG) and culturing the cells at 16 °C overnight. The cells were harvested by centrifugation, resuspended in pre-cooled lysis buffer (100 mM Tris-HCl pH 7.4, 200 mM NaCl, 1 mM MgCl$_2$, 10% glycerol, 1 mM dithiothreitol (DTT), 1 mM phenylmethylsulfonyl fluoride (PMSF), protease inhibitor mix (Roche) and 75 U ml^{-1} of Pierce universal nuclease) and processed for lysis by freezer milling (SPEX SamplePrep 6870 Freezer/Mill; five cycles of 2 min cooling and 2 min grinding at setting 15 CPS). The extracts were cleared by centrifugation (48,000g, 4 °C, 30 min), and the supernatant was loaded on a Strep-Tactin Superflow Plus column (Qiagen) at 4 °C following the manufacturer's instructions. Proteins were eluted using 2.5 mM D-desthiobiotin in purification buffer (100 mM Tris-HCl pH 7.4, 200 mM NaCl, 1 mM MgCl$_2$, 10% glycerol, 1 mM DTT and 1 mM PMSF). Fractions were collected, checked by SDS-PAGE and Coomassie blue staining, and pure fractions were pooled and aliquoted for storage at −80 °C.

Transmission electron microscopy. After thawing on ice, Cdc19 samples were cleared by centrifugation (21,000g, 4 °C, 10 min), diluted to 0.2 mg ml^{-1} in purification buffer pH 7.4 and adjusted to pH 6–7. Subsequently, a non-glow discharged carbon film 300 mesh copper grid (CF300-CU, Electron Microscopy Sciences) was submerged in this Cdc19 dilution and incubated for 10 min at 42 °C. Excess sample was then manually removed with Whatman filter paper. Where indicated, grids with pre-formed Cdc19 aggregates were incubated for 20 min with FBP or F6P dissolved in purification buffer to the indicated concentration, or simply washed twice with purification buffer, and stained with two drops of 2% uranyl acetate. A FEI Morgagni 268 microscope at 100 kV with a CCD 1,376 × 1,032 pixel camera at different magnifications was used to acquire the transmission electron micrographs.

In vitro protein-metabolite precipitation. Purified wild-type or mutant Cdc19 was thawed on ice, cleared by centrifugation (21,000g, 4 °C, 10 min) and diluted to a final protein concentration of 0.5 mg ml^{-1} in purification buffer. The different metabolites (FBP, F6P, ATP, PEP and trehalose) were solubilized in the same buffer

and added to Cdc19 to the indicated final concentrations; the protein-metabolite samples were then incubated for 14 h at 30 °C. The aggregates were pelleted by centrifugation (21,000g, 4 °C, 10 min) and separated from the supernatant containing soluble Cdc19. Aggregation was quantified by loading the pellet and supernatant on an SDS-PAGE gel, followed by Coomassie blue staining and quantification using the FIJI (ImageJ, v. 2.0.0) software.

In vitro aggregate re-solubilization with FBP. Purified wild-type Cdc19 was heat shocked for 10 min at 42 °C and the resulting aggregates were incubated with purification buffer or 20 mM FBP for 5 h at 4 °C. The aggregates were pelleted by centrifugation (21,000g, 4 °C, 10 min) and Cdc19 re-solubilization in the presence or absence of FBP was quantified by loading the supernatant and pellet fractions on an SDS-PAGE gel, followed by Coomassie blue staining.

Metabolite extraction and LC-MS/MS measurements. For metabolite extraction, 1 ml cultures were vacuum-filtered on a PVDF filter with a pore size of 0.45 µm (Millipore) and the cell pellets were immediately transferred into 4 ml of −20 °C cold extraction solution (40:40:20 acetonitrile/methanol/water; HPLC-grade solvents) supplemented with 200 µl of ^{13}C internal standard and incubated at −20 °C for 2 h. The extraction solution was centrifuged (4,000 r.p.m., 0 °C, 15 min) and the supernatant containing the metabolites was transferred to fresh tubes. The samples were dried overnight in a SpeedVac and stored at −80 °C. The samples were resuspended in 100 µl ddH$_2$O before the targeted metabolomics measurements were performed.

Compounds were analysed using a liquid chromatography with tandem mass spectrometry (LC-MS/MS) system consisting of a 1290 Infinity LC (Agilent Technologies) coupled to a 5500 QTRAP triple quadrupole mass spectrometer (AB Sciex) in negative multiple-reaction-monitoring scan mode. The metabolite extracts (5 µl) were injected on an Agilent PoroShell 120 HILIC-Z column (150 × 2.1 mm, 2.7 µm) using a mobile phase A (water, 10 mM ammonium acetate and 5 µM medronic acid, pH 9) and mobile phase B (90% acetonitrile, 10% water, 10 mM ammonium acetate and 5 µM medronic acid, pH 9) at a constant flow rate of 250 µl min^{-1}. The gradient was as follows: 10% phase A; 2 min, 10% phase A; 12 min, 40% phase A; 15 min, 40% phase A; 16 min, 10% phase A; and 24 min, 10% phase A. The multiple-reaction-monitoring settings were adapted from Yuan and colleagues[47]. The raw data were processed and analysed using a proprietary software in MatLab (Mathworks); the exact choice of software is not essential for reproducing the results.

The intracellular metabolite concentration was calculated based on the measured ^{12}C/^{13}C ratio, assuming a dry weight[48] of 0.53 g l^{-1} per OD$_{600}$ unit and a cell volume[49] of 0.0021 g^{-1}. Calibration curves were obtained from dilutions of pure compounds containing equal amounts of ^{13}C internal standard.

Protein extraction and western blotting. Proteins were precipitated using a TCA/acetone-based protocol. Briefly, exponentially growing cells were incubated for 10 min on ice after the addition of 10% TCA and centrifuged (21,000g, 4 °C, 5 min), and the pellets were washed twice with acetone. The precipitated proteins were resuspended using an SDS-based loading buffer and the protein levels were quantified by western blotting with specific antibodies. The following antibodies were used: anti-GFP (Roche, 11 814 460 001; 1:3,000 dilution), rabbit polyclonal anti-Crm1 antibody (provided by K. Weis; 1:3,000 dilution), anti-Pgk1 (Invitrogen, 459250; 1:3,000 dilution), horseradish peroxidase-coupled secondary antibody (Bio-Rad, 170-6516; 1:3,000 dilution) and anti-Hsp104 (Abcam, ab69549; 1:1,000 dilution).

Pyruvate kinase activity assay. The pyruvate kinase activity was measured with an enzymatic assay where pyruvate production by Cdc19 is coupled to lactate production by lactate dehydrogenase and the simultaneous conversion of NADH to NAD+ is measured spectrophotometrically at 340 nm. Purified Cdc19 was diluted to 0.2 mg ml^{-1} and either kept on ice or heat shocked for 60 min at 42 °C. Soluble or aggregated Cdc19 was diluted in activity buffer (50 mM imidazole pH 7, 100 mM KCl, 25 mM MgCl$_2$, 10 mM ADP, 0.3 mM NADH and 10 U ml^{-1} LDH) to a final protein concentration of 2 µg ml^{-1}. Reactions were started by adding PEP (final concentration of 2 mM) and the decrease in absorbance at 340 nm over time was monitored.

Size-exclusion chromatography. Purified wild-type or mutant Cdc19 was thawed on ice and cleared by centrifugation (21,000g, 4 °C, 10 min). Protein (0.1 mg) was loaded on a Superdex 200 10/300 GL size-exclusion column (GE Healthcare) connected to an ÄKTA pure system (GE Healthcare) at 4 °C. Protein elution was followed by the measurement of ultraviolet light absorbance (at 215 nm and 280 nm), and the collected fractions were analysed by SDS-PAGE and Coomassie blue staining.

Lysates for size-exclusion chromatography were prepared by culturing cells expressing wild-type or mutant Cdc19–GFP in SD medium to an OD$_{600}$ of 0.6. The cells were harvested by centrifugation, and the pellets were resuspended in lysis buffer (PBS buffer pH 7.4, 10% glycerol, 0.5% Tween 20, 20 mM β-glycero-phosphate, 1 mM vanadate, 1 mM NaF, 1 mM PMSF and protease inhibitor mix (Roche)), mixed with glass beads (Sigma-Aldrich, 425–600 µm)

and lysed with a FastPrep homogenizer (FastPrep-24 5G, MP Biochemicals). The resulting extracts were cleared by centrifugation (21,000g, 4 °C, 10 min) and filtering (0.2 µm filter; Millipore). The protein concentration of the supernatant was measured using a NanoDrop and a total of 4 mg protein was loaded on a Superdex 200 10/300 GL size-exclusion column (GE Healthcare) connected to an ÄKTA pure system (GE Healthcare). The column was previously equilibrated in lysis buffer and run according to the manufacturer's instructions. Fractions were collected and analysed by western blotting with anti-GFP antibodies.

Circular dichroism, Thioflavin T and Congo red staining in vitro. Circular dichroism spectra of purified wild-type or mutant Cdc19 (0.2 mg ml⁻¹) were measured using a J-710 spectropolarimeter (Jasco) and a quartz cuvette with a path length of 0.1 cm.

For in vitro measurements with the amyloid dyes, Thioflavin T (Sigma-Aldrich, T3516) or Congo red (Sigma-Aldrich, 75768-25MG) were dissolved in purification buffer to a final concentration of 2.5 mM or 1 mM, respectively, and filtered (0.2 µm; Millipore). The purified wild-type or mutant Cdc19 was thawed on ice, cleared by centrifugation (21,000g, 4 °C, 10 min), diluted to 0.3 mg ml⁻¹ in purification buffer and then either heat shocked (10 min, 42 °C) or kept on ice. Thioflavin T or Congo red solution was added (1:10 dilution) and the fluorescence intensity was measured in a 384-well plate (Corning Life Sciences) at the indicated temperature using a CLARIOstar plate reader (BMG Labtech). For Thioflavin T, excitation was set at 450 nm and emission spectra were recorded at 490 nm. For Congo red, the fluorescence intensity was measured at 614 nm with an excitation at 560 nm.

Congo red staining ex vivo. For the ex vivo Congo red staining, cells expressing wild-type or mutant Cdc19–GFP were collected by centrifugation, resuspended in lysis buffer (PBS buffer pH 7.4, 10% glycerol, 0.5% Tween 20 and 1 mM PMSF) and lysed at 4 °C with glass beads (Sigma-Aldrich; 425–600 µm) and a FastPrep homogenizer (FastPrep-24 5G, MP Biochemicals). The lysates were cleared by centrifugation (2,000g, 4 °C, 2 min) and the total protein concentration was determined using a NanoDrop. Glass microscopy slides were cleaned with consecutive washes of H₂O, 100% ethanol and acetone, before 3 mm-wide stripes of double-sided tape were applied along the length of the glass slides to form three channels (approximatively 3 mm-wide). The assembled flow chambers were functionalized by incubation for 20 min with 0.3 mg ml⁻¹ Avidin DN (Vector Laboratories) in T50 buffer (10 mM Tris pH 8.0 and 50 mM NaCl), blocked for 30 min with 0.1% puronic F-127 (Sigma-Aldrich) in T50 buffer, washed twice with 0.1 mg ml⁻¹ BSA in T50 buffer and incubated for 30 min with biotinylated G-protein in lysis buffer. Finally, 10 nM anti-GFP in lysis buffer was flushed into the channels, and the protein extracts were loaded and allowed to bind for 10 min, before washing three times with lysis buffer. The aggregates were stained with 250 µM Congo red in lysis buffer, excess dye was removed by washing twice with lysis buffer and the aggregates were analysed by fluorescence microscopy.

LiP-MS experiments, SRM assays and quantification analysis. For the in vivo LiP-MS experiments, cells expressing Cdc19^WT–GFP or Cdc19^irrev–GFP were cultured in SD medium and three biological replicates were collected when the cells were growing exponentially (OD₆₀₀ of 0.6) or following entry into stationary phase (2 d). The cells were resuspended in 100 mM HEPES, 150 mM KCl and 1 mM MgCl₂ (pH 7.6), and disrupted by bead beating in the presence of acid-washed glass beads in three consecutive rounds of 30 s of beating and 4 min of incubation at 4 °C. The protein concentration in the yeast extracts was determined using the bicinchoninic acid assay (BCA protein assay kit, Thermo Scientific). Equal amounts of cell lysates were treated with proteinase K (Sigma-Aldrich) at a lysate/protease ratio of 100:1 for 3 min. Protease activity was quenched by heating at 95 °C and adding 5% sodium deoxycholate (Sigma-Aldrich)[50]. Equal amounts of cell lysates were treated in parallel with vehicle instead of proteinase K to estimate the variation in Cdc19 protein amounts in the different conditions assayed. Tris(2-carboxyethyl)phosphine-HCl (Thermo Fisher Scientific) was added to a final concentration of 5 mM (35 min, 37 °C) to reduce disulfide bridges, followed by alkylation of free cysteine residues with iodoacetamide (Sigma-Aldrich) at a final concentration of 20 mM (30 min, room temperature). The peptide and protein fragments were digested to completion in denaturing conditions with LysC and trypsin proteases. Before adding LysC and trypsin, the reaction mixtures were diluted with 0.1 M ammonium bicarbonate (Sigma-Aldrich) to reach a sodium deoxycholate concentration of <1%. First, LysC digestion was performed at an enzyme/substrate ratio of 1:100 for 4 h at 37 °C, then trypsin digestion was carried out at an enzyme/substrate ratio of 1:100 for 16 h at 37 °C. For the LiP experiments with recombinantly purified proteins, aliquots of recombinantly purified Cdc19^WT and Cdc19^irrev were incubated for 10 min at 25 °C or 42 °C in triplicates to induce Cdc19 structural variations just before the limited proteolysis step.

The development and validation of the Selected Reaction Monitoring (SRM) assays to measure Cdc19 levels were guided by a spectral library generated in-house through an LC–MS/MS analysis of the in vivo yeast samples on a QE-plus (Thermo Fisher Scientific) mass spectrometer equipped with a nano-electrospray ion source. On-line chromatographic separation of the peptides was achieved with an Easy-nLC 1000 nano liquid chromatography system (Thermo Fisher

Scientific) equipped with a 40 cm fused-silica column (New Objective), packed in-house with Reprosil Pur C18 Aq, 1.9 µm beads (Dr Maisch). The peptide mixtures (approximately 1 µg) were separated with a linear gradient from 5% to 35% acetonitrile in 120 min. The collected spectra were searched against the *Saccharomyces cerevisiae* UniProt reference database using Sorcerer-Sequest (Thermo Electron). Trypsin was set as the digesting protease tolerating two missed cleavages and semi-tryptic termini. Cysteine carbamidomethylation (+57.0214 Da) was defined as a fixed modification and methionine oxidation (+15.99492 Da) as a variable modification. Protein identifications were filtered with a false-discovery rate of <1%, calculated on the basis of a target-decoy approach. Proteome Discoverer 2.2 (Thermo Fisher Scientific) was used to build a consensus spectral library using LiP-MS in vivo samples.

Peptides matching to the spectral library were ranked by intensity using Skyline (v4.1; MacCoss Lab Software, University of Washington) and the ten most intense transitions consisting of doubly or triply charged precursor ions and singly or doubly charged fragment ions of the y- and b-ion series were experimentally tested in SRM mode to select the most suitable transitions for quantification. Samples were measured on a triple quadrupole/ion-trap mass spectrometer (5500 QTrap, AB Sciex) equipped with a nano-electrospray ion source and operated in SRM mode. On-line chromatographic peptide separation was achieved with an Eksigent 1D-plus Nano liquid chromatography system equipped with a 15 cm fused-silica column with an inner diameter of 75 µm, packed in-house with Reprosil Pur C18 Aq, 5 µm beads (Dr Maisch). The peptide mixtures (approximately 1 µg) were separated with a linear gradient from 5% to 35% acetonitrile in 30 min. The SRM analysis was conducted with Q1 and Q3 operated at unit resolution (0.7 m/z half-maximum peak width) with a dwell time of 20 ms and a cycle time <3.0 s.

The SRM mass spectrometry data were analysed using Skyline, and for the final SRM assay, retention times were scheduled and at least three transitions per precursor ion of Cdc19 were retained. The identity of each SRM peak was confirmed against the spectral library by matching realigned retention times and relative fragment-ion intensities. 199 transitions matching to 44 Cdc19 precursors were selected for Cdc19 peptide quantification purposes. Integration of peak areas was manually inspected and relative quantification was performed for the Cdc19 peptides in the LiP-MS in vitro and in vivo experiments. Statistical significance analysis was performed using MSstats (www.msstats.org). Precursor intensities were normalized using the option 'equalize medians' of MSstats. In the LiP-MS in vivo experiments, peptide intensities were corrected for variations of Cdc19 protein levels between the exponential and stationary conditions. The normalization factor applied was equivalent to the relative variation of the Cdc19^WT or Cdc19^irrev proteins between the exponential and stationary conditions.

Statistics and reproducibility. All data are representative results from at least three independent experiments, unless otherwise specified in the figure legends. Whenever possible, the mean ± s.e.m. and individual data points of individual experiments are shown. GraphPad Prism was used to analyse and plot data. No statistical method was used to predetermine sample size and the experiments were not randomized. No outlier tests were performed and no data were excluded from the analyses. The investigators were not blinded to allocation during the experiments and outcome assessment.

Reporting Summary. Further information on research design is available in the Nature Research Reporting Summary linked to this article.

Data availability

Mass spectrometry data have been deposited to the ProteomeXchange Consortium via the PRIDE[51] partner repository (dataset identifier PXD026060). Numerical source data giving rise to graphical representations (with all independent repeats) and unprocessed images of gels and blots are reported in the Source Data files. Detailed experimental procedures and additional data supporting the findings of this study are available from the corresponding author upon reasonable request. Source data are provided with this paper.

References

47. Yuan, M. et al. A positive/negative ion-switching, targeted mass spectrometry-based metabolomics platform for bodily fluids, cells, and fresh and fixed tissue. *Nat. Protoc.* **7**, 872–881 (2012).
48. Sonderegger, M. & Sauer, U. Evolutionary engineering of *Saccharomyces cerevisiae* for anaerobic growth on xylose. *Appl. Environ. Microbiol.* **69**, 1990–1998 (2003).
49. Lamprecht, I., Schaarschmidt, B. & Welge, G. Microcalorimetric investigation of the metabolism of yeasts. V. Influence of ploidy on growth and metabolism. *Radiat. Environ. Biophys.* **13**, 57–61 (1976).
50. Piazza, I. et al. A map of protein-metabolite interactions reveals principles of chemical communication. *Cell* **172**, 358–372 (2018).
51. Perez-Riverol, Y. et al. The PRIDE database and related tools and resources in 2019: improving support for quantification data. *Nucleic Acids Res.* **47**, D442–D450 (2019).

Author contributions

Conceptualization: G.C., R.D. and M.P. Formal analysis: G.C. and I.P. Investigation: G.C., C.W.-Z., V.M.K., M.D., A.A., I.P., H.Y. and S.S. Writing–original draft preparation: G.C. and M.P. Writing–review and editing: G.C. and M.P., with input from all authors. Visualization: G.C. and M.P. Supervision: M.P., P.P., U.S. and D.A.D. Funding acquisition: M.P., P.P., U.S. and D.A.D.

Competing interests
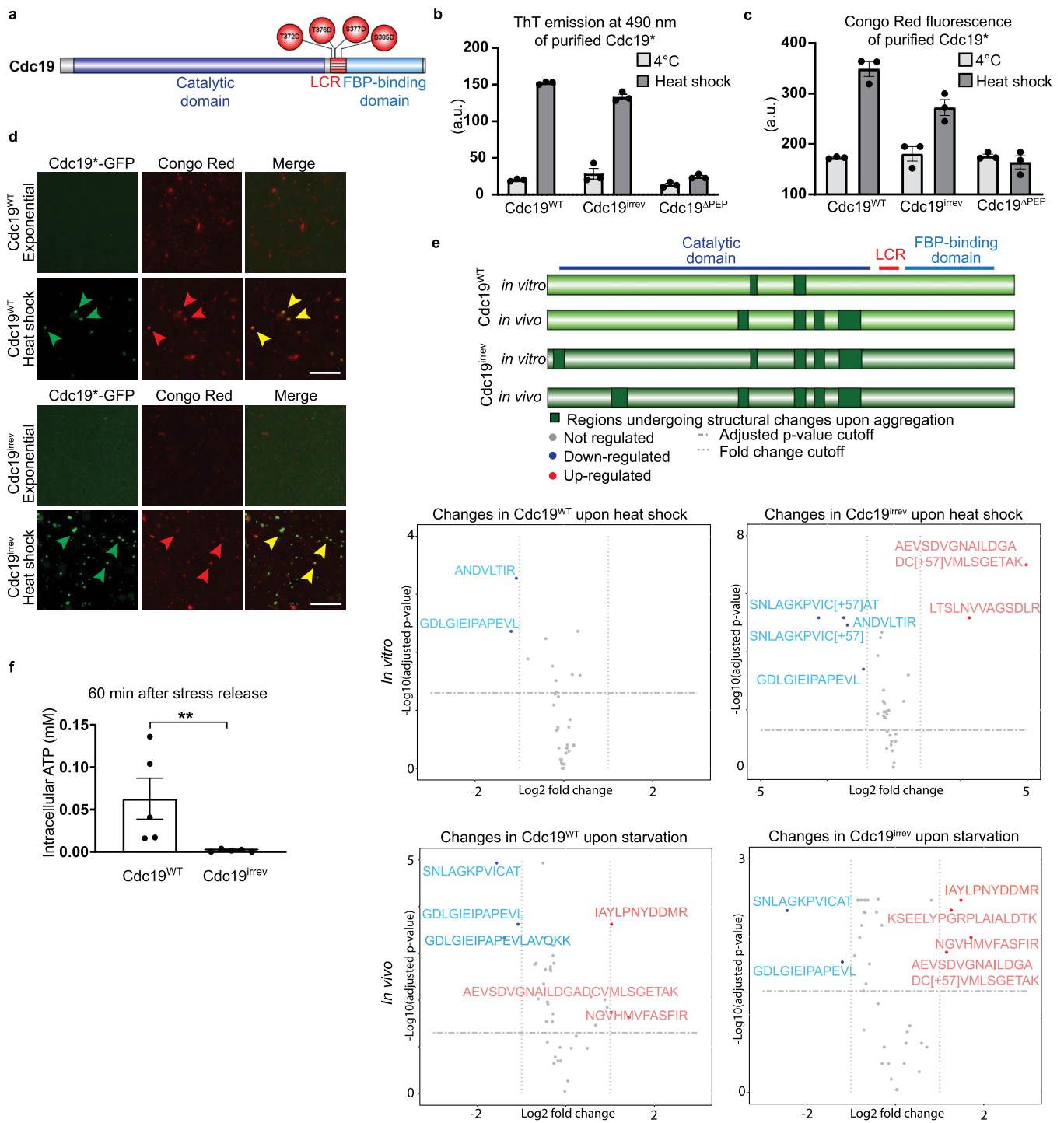
The authors declare no competing interests.

Additional information

Extended data is available for this paper at https://doi.org/10.1038/s41556-021-00760-4.

Supplementary information The online version contains supplementary material available at https://doi.org/10.1038/s41556-021-00760-4.

**Correspondence and requests for materials** should be addressed to Matthias Peter.

Peer review information *Nature Cell Biology* thanks the anonymous reviewers for their contribution to the peer review of this work. Peer reviewer reports are available.

Reprints and permissions information is available at www.nature.com/reprints.

a Cdc19 — Catalytic domain, LCR, FBP-binding domain (T372D, T376D, S377D, S385D)

b ThT emission at 490 nm of purified Cdc19*

c Congo Red fluorescence of purified Cdc19*

d Cdc19*-GFP / Congo Red / Merge — Cdc19WT Exponential, Cdc19WT Heat shock, Cdc19irrev Exponential, Cdc19irrev Heat shock

e Regions undergoing structural changes upon aggregation; Not regulated; Down-regulated; Up-regulated; Adjusted p-value cutoff; Fold change cutoff

Changes in Cdc19WT upon heat shock
Changes in Cdc19irrev upon heat shock
Changes in Cdc19WT upon starvation
Changes in Cdc19irrev upon starvation

f 60 min after stress release — Intracellular ATP (mM): Cdc19WT, Cdc19irrev **

Extended Data Fig. 1 | See next page for caption.

Extended Data Fig. 1 | Cdc19 aggregates are amyloids both in vitro and in vivo. a, Schematic representation of the domains of Cdc19. The four mutated residues located within the LCR in the Cdc19^{irrev} mutant are indicated (red circles). **b,c**, Both Cdc19^{WT} and Cdc19^{irrev} form ThT- and Congo Red (CR)-positive aggregates upon heat shock in vitro. Purified Cdc19^{WT}, Cdc19^{irrev} and a non-aggregating Cdc19 mutant as negative control (Cdc19$^{\Delta PEP4}$) were incubated with ThT **(b)** or CR **(c)** at 4 °C or after heat shock (42 °C, 10 min). Fluorescence emission was measured at 490 nm or 614 nm, respectively. The mean ± s.e.m. is shown ($n = 3$ independent experiments, two-tailed t-tests, ThT: $P_{WT} = 0.0000149$, $P_{irrev} = 0.0091$, CR: $P_{WT} = 0.0003$, $P_{irrev} = 0.0128$). **d**, In vivo-formed Cdc19^{WT} and Cdc19^{irrev} aggregates are CR-positive. Cells expressing GFP-tagged Cdc19^{WT} or Cdc19^{irrev} were harvested when exponentially growing or after heat shock (42 °C, 30 min) and lysed. Cdc19–GFP was immobilized in a GFP-trap microfluidic chamber and stained with CR. GFP and CR signals were detected by fluorescence microscopy, and merged to visualize co-localization. Arrowheads indicate CR-positive Cdc19–GFP aggregates ($n = 3$ independent experiments). Scale bars; 10 μm. **e**, Limited-Proteolysis Mass Spectrometry (LiP-MS) results indicate that Cdc19^{WT} and Cdc19^{irrev} undergo comparable structural transitions upon aggregation in vitro and in vivo. Purified soluble or aggregated (42 °C, 10 min) Cdc19^{WT} or Cdc19^{irrev}, as well as cell extracts obtained from cells expressing Cdc19^{WT}-GFP or Cdc19^{irrev}-GFP harvested during exponential growth or stationary phase (2 d) to induce aggregation were analysed by LiP-MS as described in the Methods ($n = 3$ independent experiments). Peptides detected in soluble and aggregated Cdc19^{WT} and Cdc19^{irrev} are displayed in volcano plots, and upregulated (red) or downregulated (blue) conformation-sensitive peptides are highlighted. Conformation-specific LiP-MS-peptides detected in vitro and in vivo were mapped to the Cdc19 schematic drawing (green). **f**, Intracellular ATP levels (mM) were determined in the indicated strains after heat shock (42 °C, 30 min) and recovery (30 °C, 60 min). The mean ± s.e.m. of $n = 5$ independent experiments is shown (two-tailed Mann-Whitney test, **$P = 0.0079$); a.u., arbitrary units. Source data for all graphical representations are found in Source Data Extended Data Fig. 1.
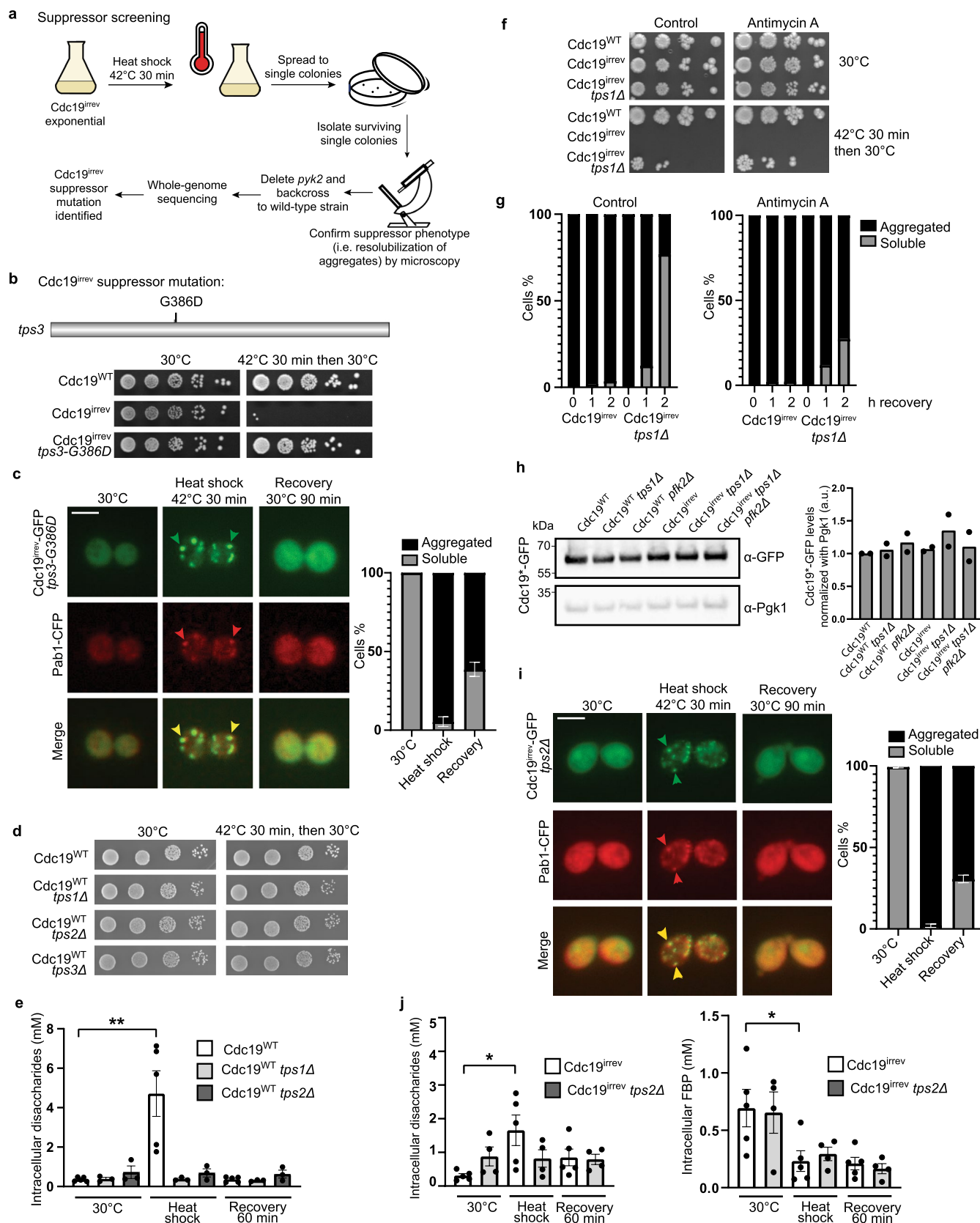
Extended Data Fig. 2 | See next page for caption.

Extended Data Fig. 2 | Genetic screening identifies trehalose metabolism as a regulator of reversible Cdc19 aggregation. a, Screening protocol that identified a single point mutation (G386D) in *TPS3* as a suppressor of stress-induced growth arrest of *cdc19*[irrev] cells. **b,d**, Serial dilutions of the indicated exponentially growing strains were spotted on agar plates before or after heat shock (42 °C, 30 min), and imaged after 3 d at 30 °C ($n = 3$ independent experiments). **c**, Exponentially growing *tps3-G385D* cells expressing Cdc19[irrev]-GFP and Pab1–CFP were cultivated at 30 °C, then heat shocked (42 °C, 30 min) and allowed to recover at 30 °C. The mean ± s.e.m. percentage of cells with Cdc19 aggregates is indicated ($n = 3$ independent experiments, >30 cells per sample per experiment). Scale bar; 5 μm. **e**, Intracellular disaccharides were measured in the indicated strains before, during and after heat shock (42 °C, 30 min). The mean ± s.e.m. is shown ($n = 5$ independent experiments for wild-type, $n = 3$ independent experiments for *tps1Δ* and *tps2Δ*, two-tailed Mann-Whitney test, **$P = 0.0079$). **f,g**, The indicated exponentially growing strains were heat shocked (42 °C, 30 min) and allowed to recover at 30 °C ± antimycin A (1 or 2 μM, respectively). **f**, Serial dilutions were spotted on agar plates ± antimycin A before or after heat shock, and imaged after 3 d at 30 °C ($n = 3$ independent experiments). **g**, Plots indicate mean percentage of cells that re-solubilized Cdc19 ($n = 2$ independent experiments). **h**, Mean Cdc19–GFP levels relative to Pgk1 in the indicated strains are shown ($n = 2$ independent experiments). **i**, Exponentially growing *tps2Δ* cells expressing Cdc19[irrev]--GFP and Pab1–CFP were heat shocked (42 °C, 30 min) and allowed to recover at 30 °C. Plot indicates the mean ± s.e.m. percentage of cells with Cdc19 aggregates ($n = 3$ independent experiments, >30 cells per sample per experiment). Scale bar; 5 μm. **j**, Intracellular disaccharides (mainly trehalose[46]) and FBP were measured in the indicated strains before, during and after heat shock (42 °C, 30 min), and plotted as mean ± s.e.m. ($n = 4$ independent experiments for *cdc19*[irrev] *tps2Δ*, $n = 5$ for *cdc19*[irrev], two-tailed Mann-Whitney test, *$P_{Disaccharides} = 0.0159$, *$P_{FBP} = 0.0317$); a.u., arbitrary units. Source data for all graphical representations and unprocessed western blots available in Source Data Extended Data Fig. 2.
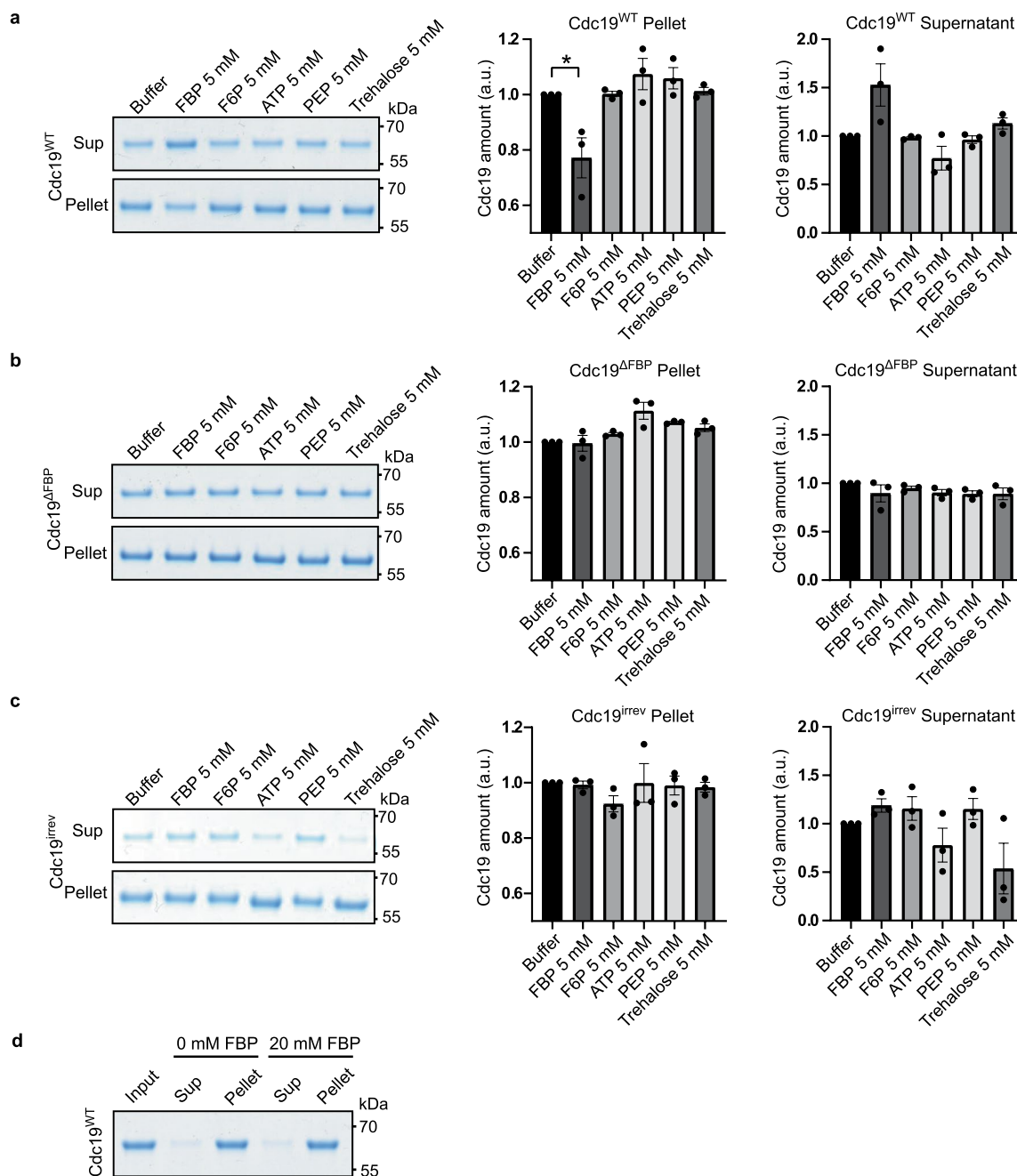
Extended Data Fig. 3 | FBP specifically reduces aggregation of purified Cdc19^{WT} but not Cdc19$^{\Delta FBP}$ and Cdc19^{irrev} mutant proteins. a–c, Purified wild-type Cdc19 **(a)**, FBP binding-deficient Cdc19$^{\Delta FBP}$ mutant **(b)** or Cdc19^{irrev} mutant **(c)** proteins were mixed as indicated with 5 mM FBP or for control 5 mM F6P, 5 mM ATP, 5 mM PEP, 5 mM trehalose or buffer and incubated at 30 °C for 14 h. Cdc19 aggregates were separated from soluble protein by centrifugation and the supernatant (Sup) and pellet fractions were analysed by SDS-PAGE and Coomassie blue staining. The amount of Cdc19 was quantified in the pellet and supernatant by measuring Cdc19 band intensities using ImageJ and normalizing to buffer controls, and is displayed as mean ± s.e.m. ($n = 3$ independent experiments, two-tailed t-test, *$P = 0.0342$). **d**, Addition of FBP alone is not sufficient to re-solubilize pre-formed Cdc19^{WT} amyloids in vitro. Purified Cdc19^{WT} (Input) was incubated for 10 min at 42 °C to trigger its aggregation, and the resulting amyloids were incubated with (20 mM) or without (0 mM) FBP for several hours. Cdc19 re-solubilization was then tested by centrifugation and analysis of the resulting supernatant (Sup) and pellet fractions by SDS-PAGE and Coomassie blue staining ($n = 3$ independent experiments); a.u., arbitrary units. Unprocessed original scans of gels are shown in Source Data Extended Data Fig. 3.
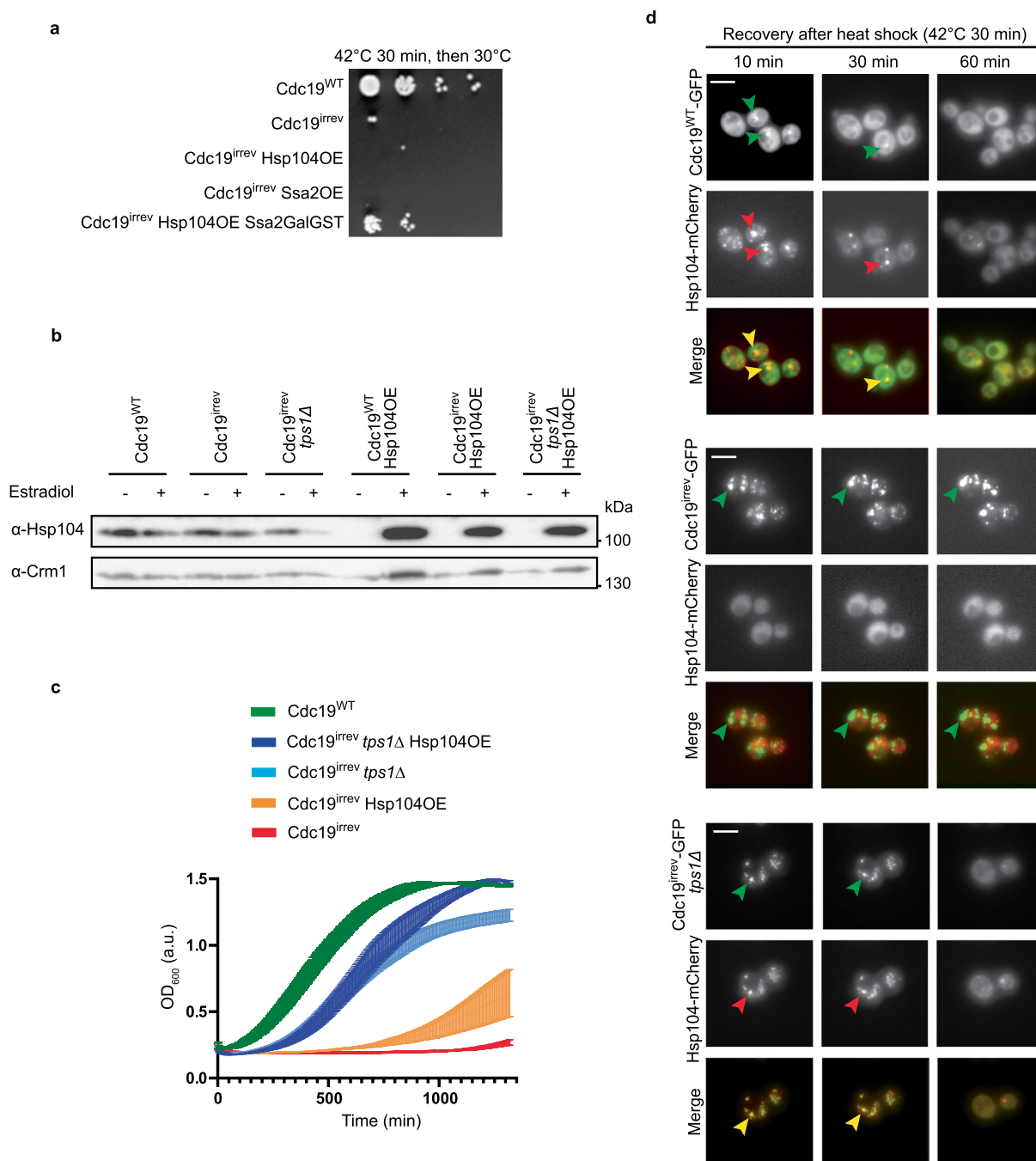
Extended Data Fig. 4 | The chaperones Hsp104 and Ssa2 cooperate with FBP to efficiently disassemble Cdc19 amyloids in vivo. a, Co-overexpression of Hsp104 and Ssa2 partially restores growth of *cdc19irrev* cells after heat stress. Wild-type and *cdc19irrev* cells overexpressing as indicated Hsp104 or Ssa2, or both together by addition of 10 mM estradiol for 3 h, were heat-shocked for 30 min at 42 °C. Serial dilutions were spotted on agar plates and grown at 30 °C for 3 d ($n = 3$ independent experiments). **b**, Hsp104 protein levels were quantified in the indicated strains by western blotting either in the absence (-) or presence (+) of 10 mM estradiol for 3 h ($n = 3$ independent experiments). **c**, Increased FBP levels and Hsp104 cooperate to efficiently restart growth after stress in *cdc19irrev* cells. Exponentially growing wild-type or *tps1Δ* cells expressing either Cdc19WT or Cdc19irrev were subjected to a 30 min heat shock at 42 °C. Where indicated, overexpression of Hsp104 was induced by treating cells with 10 mM estradiol for 3 h. Growth restart after stress release of the indicated strains was quantified by measuring the cell density (OD$_{600}$) over time after inoculation of equal cell numbers at 30 °C. Mean ± s.e.m. cell density 22 h after stress release is shown ($n = 3$ independent experiments). Note that Hsp104 overexpression and increased FBP levels cooperate to rescue *cdc19irrev* cells after heat shock. **d**, Wild-type or *tps1Δ* cells co-expressing mCherry-tagged Hsp104 and either GFP-tagged Cdc19WT or Cdc19irrev mutant were heat shocked (42 °C, 30 min), and imaged by fluorescence microscopy at the times indicated. Representative GFP- (left row) and mCherry images (middle row) are shown, together with the merged image (bottom row) to visualize co-localization of Cdc19 aggregates and Hsp104 ($n = 3$ independent experiments). Scale bars; 5 μm; a.u., arbitrary units. Source data for the graphical representation and unprocessed western blots can be found in Source Data Extended Data Fig. 4.

Corresponding author(s):   Prof. Matthias Peter

Last updated by author(s):   Aug 8, 2021

Reporting Summary

Nature Research wishes to improve the reproducibility of the work that we publish. This form provides structure for consistency and transparency in reporting. For further information on Nature Research policies, see our Editorial Policies and the Editorial Policy Checklist.

Statistics

For all statistical analyses, confirm that the following items are present in the figure legend, table legend, main text, or Methods section.

n/a	Confirmed	
☐	☒	The exact sample size (*n*) for each experimental group/condition, given as a discrete number and unit of measurement
☐	☒	A statement on whether measurements were taken from distinct samples or whether the same sample was measured repeatedly
☐	☒	The statistical test(s) used AND whether they are one- or two-sided
		Only common tests should be described solely by name; describe more complex techniques in the Methods section.
☒	☐	A description of all covariates tested
☒	☐	A description of any assumptions or corrections, such as tests of normality and adjustment for multiple comparisons
☐	☒	A full description of the statistical parameters including central tendency (e.g. means) or other basic estimates (e.g. regression coefficient) AND variation (e.g. standard deviation) or associated estimates of uncertainty (e.g. confidence intervals)
☐	☒	For null hypothesis testing, the test statistic (e.g. *F*, *t*, *r*) with confidence intervals, effect sizes, degrees of freedom and *P* value noted
		Give P values as exact values whenever suitable.
☒	☐	For Bayesian analysis, information on the choice of priors and Markov chain Monte Carlo settings
☒	☐	For hierarchical and complex designs, identification of the appropriate level for tests and full reporting of outcomes
☒	☐	Estimates of effect sizes (e.g. Cohen's *d*, Pearson's *r*), indicating how they were calculated

Our web collection on statistics for biologists contains articles on many of the points above.

Software and code

Policy information about availability of computer code

Data collection	Microscopy Images were acquired using MicroManager V 1.4 and NIS-Elements Advanced Research, V 5.02.
Data analysis	Image processing for microscopy, gels and western blots: FIJI (ImageJ V 2.0.0).
	Statistics and visualization: Graphpad Prism 8, Excel for Windows Version 16.38, Matlab R2018b
	LiP-MS: Skyline v4.1
	Metabolomics: the raw metabolomics data were processed with a proprietary software, the exact choice of software is not essential for reproducing the results. Since many equivalent custom and commercial software exist to do this data processing, deposition of this code in a public database is not necessary to reproduce the data presented in this work.

For manuscripts utilizing custom algorithms or software that are central to the research but not yet described in published literature, software must be made available to editors and reviewers. We strongly encourage code deposition in a community repository (e.g. GitHub). See the Nature Research guidelines for submitting code & software for further information.

Data

Policy information about availability of data

All manuscripts must include a data availability statement. This statement should provide the following information, where applicable:
- Accession codes, unique identifiers, or web links for publicly available datasets
- A list of figures that have associated raw data
- A description of any restrictions on data availability

Mass spectrometry data have been deposited to the ProteomeXchange Consortium via the PRIDE [Perez-Riverol, Y., et al., Nucleic Acids Res, 2019. 47(D1): p. D442-d450] partner repository (dataset identifier PDX026060). Numerical source data giving rise to graphical representations, with all independent repeats, are reported

in Excel format in Suppl. Table S3. Unprocessed images of gels and blots are shown in Suppl. Fig. 5 and 6. Detailed experimental procedures and additional data supporting the findings of this study are available from the corresponding authors upon request.

Field-specific reporting

Please select the one below that is the best fit for your research. If you are not sure, read the appropriate sections before making your selection.

☒ Life sciences   ☐ Behavioural & social sciences   ☐ Ecological, evolutionary & environmental sciences

For a reference copy of the document with all sections, see nature.com/documents/nr-reporting-summary-flat.pdf

Life sciences study design

All studies must disclose on these points even when the disclosure is negative.

Sample size	No statistical method was used to predetermine sample size. Standard considerations based on expected variations form previous experiments [Saad et al., NCB, 2017, DOI: 10.1038/ncb3600] were applied to determine the necessary repeats to ensure reproducibility and statistical significance. All experiments were performed with at least 3 biological replicates (exception: Western blot in Suppl. Fig. 2H and quantification in Suppl. Fig. 2G were repeated only twice). At least 30 individual cells per condition/time point and experiment/replica have been included in the analysis (as stated in the corresponding Figure legends).
Data exclusions	No outlier tests were performed, no data were excluded from the analysis.
Replication	All shown data are representative results from at least three independent experiments (exception: Western blot in Suppl. Fig. 2H and quantification in Suppl. Fig. 2G were repeated only twice). At least 30 individual cells per condition/time point and experiment/replica have been included in the analysis (as stated in the corresponding Figure legends).
Randomization	No randomization has been performed, as this was not a case/control study including individual participants. Samples were derived from genetically identical, single colonies.
Blinding	No blinding of investigators has been performed. The outcome and assessment of the reported results could not be influenced by the knowledge of the investigators in a relevant way. This study is assessing outcomes which can be analyzed in an objective, reliable and repeatable way. Moreover, our findings are substantiated by orthogonal experiments, strongly ensuring reproducibility and reliability.

Reporting for specific materials, systems and methods

We require information from authors about some types of materials, experimental systems and methods used in many studies. Here, indicate whether each material, system or method listed is relevant to your study. If you are not sure if a list item applies to your research, read the appropriate section before selecting a response.

Materials & experimental systems

n/a	Involved in the study
☐	☒ Antibodies
☒	☐ Eukaryotic cell lines
☒	☐ Palaeontology and archaeology
☒	☐ Animals and other organisms
☒	☐ Human research participants
☒	☐ Clinical data
☒	☐ Dual use research of concern

Methods

n/a	Involved in the study
☒	☐ ChIP-seq
☒	☐ Flow cytometry
☒	☐ MRI-based neuroimaging

Antibodies

Antibodies used	The following commercially available antibodies were used: α-GFP (Roche, 11 814 460 001, dilution 1:3000), α-Pgk1 (Invitrogen, 459250, dilution 1:3000), HRP-coupled secondary antibody (Biorad, 170-6516, dilution 1:3000) and α-Hsp104 (Abcam, ab69549, dilution 1:1000). Moreover, we used a rabbit polyclonal α-Crm1 antibody, kindly provided by Prof. Karsten Weis (1:3000 dilution).
Validation	Antibodies purchased from Roche, Invitrogen, Biorad and Abcam were validated in multiple previous studies (accessible at https://www.sigmaaldrich.com/, https://www.thermofisher.com/, https://www.bio-rad.com/, https://www.abcam.com/) and by the manufacturers.